

Remote Sensing Change Detection via Weak Temporal Supervision

Xavier Bou¹ * Elliot Vincent² * Gabriele Facciolo¹

Rafael Grompone von Gioi¹ Jean-Michel Morel³ Thibaud Ehret⁴

¹Université Paris-Saclay, CNRS, ENS Paris-Saclay, Centre Borelli, France

²LASTIG, Université Gustave Eiffel, IGN-ENSG, France

³Lingnan University, Hong Kong ⁴AMIAD, Pole Recherche, France

<https://xavibou.github.io/CDviaWTS/>

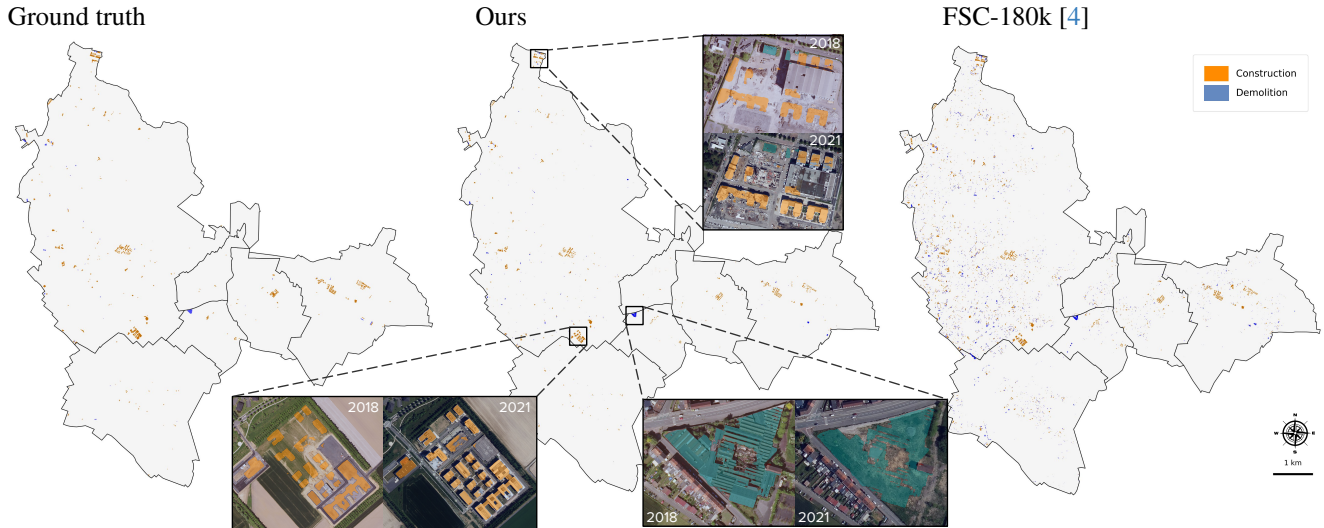


Figure 1. **Large-scale building change detection comparison on BD ORTHO [29] data (Lille metropolitan area in France, approximately 55.3 km²).** Availability of annotated datasets has always been a challenge for semantic change detection. To avoid this problem, we propose a novel weak temporal supervision strategy that leverages additional temporal observations of existing single-date annotated data. This allows us to train robust and scalable models, without requiring any new annotations. Left: map presenting the reference building changes (demolitions and constructions) derived from the French IGN's OCS GE data product [30]. Middle: result of a Dual UNet trained with our methodology, which closely aligns with the reference. Right: output of a Dual UNet trained on FSC-180k [4], which produces numerous false positives.

Abstract

Semantic change detection in remote sensing aims to identify land cover changes between bi-temporal image pairs. Progress in this area has been limited by the scarcity of annotated datasets, as pixel-level annotation is costly and time-consuming. To address this, recent methods leverage synthetic data or generate artificial change pairs, but out-of-domain generalization remains limited. In this work, we introduce a weak temporal supervision strategy that leverages additional temporal observations of existing single-temporal

datasets, without requiring any new annotations. Specifically, we extend single-date remote sensing datasets with new observations acquired at different times and train a change detection model by assuming that real bi-temporal pairs mostly contain no change, while pairing images from different locations to generate change examples. To handle the inherent noise in these weak labels, we employ an object-aware change map generation and an iterative refinement process. We validate our approach on extended versions of the FLAIR and IAIID aerial datasets, achieving strong zero-shot and low-data regime performance across different benchmarks. Lastly, we showcase results over large areas in France, highlighting the scalability potential of our method.

* These authors contributed equally

1. Introduction

Detection and monitoring of changes in remote sensing data remain a central topic within the Earth observation community over recent years [16]. A wide range of applications emerge from remote sensing change detection, including natural disaster damage assessment [5, 7, 17], urban development monitoring [28, 67], or deforestation detection [37, 66]. In particular, the task of bi-temporal change detection consists in finding the semantic differences between a pair of co-registered satellite or aerial images acquired at different dates, given a set of land cover classes of interest.

State-of-the-art methods for this task use deep neural networks [15, 24, 48, 57] trained on datasets of image pairs annotated with pixel-level change maps [14, 33, 54, 69] or even semantic maps at both dates [10, 61]. Nevertheless, gathering such data is both expensive and time consuming. As a result, change detection data is often spatially or temporally clustered, and methods trained on them hardly generalize to new, unseen locations. To address the scarcity of labeled data, several works have attempted to train change detection models in an unsupervised [11, 47] or weakly supervised fashion [72], learning from much cheaper image-level annotations. However, these methods still lag behind fully supervised approaches, particularly in the spatial accuracy of predicted changes.

To benefit from quality semantic annotations at a larger scale, several works attempt to leverage single-temporal annotated datasets in order to train change detection model. This is the case of synthetic change datasets generated from such existing data [4], but also of learning frameworks considering non-overlapping images as training pairs [52, 72], pairing images from different locations and thus generating *fake change pairs*. However, such attempts do not take advantage of the growing availability of remote sensing data. Satellite and aerial image acquisition campaigns are indeed often programmed to occur regularly by national GIS institutes [29, 63] or to last a long period of time by spatial agencies [46, 60].

In this paper, we propose to expand single-date semantic segmentation datasets into bi-temporal collections, leveraging easily accessible imagery. We introduce a new weakly supervised paradigm, where only single-temporal semantic maps are available to train a change detection network on bi-temporal pairs. Introducing this temporal variability exposes the model to naturally occurring variations that do not constitute semantically meaning changes, making it more robust. Because this weak temporal supervision is by nature noisy, we propose three key training ideas. First, we balance real bi-temporal pairs and fake non-overlapping pairs during training. Secondly, inspired by [72], we supervised fake pairs with an sIoU-based [12, 51] change map. Third, we iteratively clean the extended dataset, filtering out real pairs exhibiting land-cover changes, so that such pairs can

be considered as unchanged during training.

We validate our methodology by expanding two existing datasets, FLAIR [26] and IAILD [45]. Through several experiments, we demonstrate that one can use additional temporal acquisitions in addition to semantic segmentation datasets to improve change detection with zero labeling cost. Our contributions are summarized as follows:

- We extend FLAIR and IAILD datasets from single-date to bi-temporal and release them for anyone to use. We additionally curate and release a test set for in-domain evaluation of building change detection methods trained on our extension of FLAIR.
- We develop an approach to leverage the additional, non-annotated images for training a change detection network.
- Through extensive experiments on several datasets, we show that our method improves the performance of change detection models. Thus, we demonstrate strong zero-shot performance, impressive low-data regime results, and compelling large-scale qualitative results, shown in Fig. 1.

2. Related Works

In this paper, we tackle the problem of detecting land cover changes in bi-temporal remote sensing image pairs. We refer to this task as semantic change detection (SCD).

Semantic change detection. Over the past few years, SCD in remote sensing images has gained significant interest, leading to a large number of publications on the topic and several field surveys [2, 16, 38, 53]. Most state-of-the-art methods rely on deep learning in order to train 3-branch neural networks. First introduced by Daudt *et al.* [21], such architectures output, for a given bi-temporal image pair, a triplet consisting of two semantic maps and a binary change map. Multiple variants [20, 23, 24, 34, 40, 42, 43, 68–70, 73] improve different aspects of the procedure, including the multitask objective [20, 73], the fusion mechanisms [34, 68], the consistency between the three outputs [24], the quality of the predicted change boundaries [42, 43], or the computational cost [40]. All these methods require pixel-level annotated image pairs in order to train a model in a fully supervised manner. Because gathering such labeled data is costly and time-consuming, we instead propose a weakly supervised framework based on single-temporal annotations, leveraging new temporal images without additional annotation cost.

Weakly supervised change detection. Weakly supervised learning encompasses any training algorithm that enables performing different or more complex tasks than typically possible with the available data. However, in the context of SCD, it specifically describes methods that infer pixel-level change predictions from weak image-level labels [1, 36, 65, 71]. For instance, Andermatt *et al.* [1] train a SCD model with image-level labels such as “forests to agricultural surfaces” for a given image pair. Between image- and pixel-level supervision, other weak signals such

as bounding boxes or coarse masks [22, 41, 64], noisy labels [9], and low-resolution annotations [39] have been used to train SCD networks. Toker *et al.* presented DynamicEarthNet [62], a dataset of daily satellite image time series for which only the first image of each month is annotated, with a focus on semi- rather than weak supervision. Beyond this work, and to the best of our knowledge, weak settings in which semantic information is completely missing for one image of the pair are often overlooked in the literature, despite corresponding to cases that commonly occur in practice due to the recurrent acquisition of imagery by space and GIS agencies.

Leveraging single-temporal annotated data. Due to the high cost of pixel-level change annotations, several works have explored leveraging single-temporal semantic segmentation datasets to enable change detection without requiring ground truth change labels. A common approach is post-classification change detection, often referred to as “the most obvious method of change detection” [55]. It compares the outputs of a single-temporal segmentation model on each image of a bi-temporal pair. In this case, multi-temporal acquisitions may serve as data augmentation at training time [3]. However, this method suffers from prediction error accumulation and lacks temporal modeling [59]. Other methods construct artificial change pairs by randomly pairing images from different locations and computing change maps based on label differences, *e.g.* STAR [72] or [52]. Another line of work consists in creating synthetic SCD datasets based on a single-temporal land cover real-world dataset, using techniques such as GANs [52, 74], or diffusion [4, 58, 75]. Building on the observation that annotation is significantly more expensive than data acquisition itself, we instead propose to extend existing single-temporal datasets with new, aligned temporal acquisitions, using their existing annotations as weak supervision for bi-temporal change detection.

3. Methodology

We focus on learning to detect changes from a single-temporal satellite or aerial image dataset annotated for the semantic segmentation task. Based on the observation that accessing new acquisitions is less costly than obtaining change labels, our pipeline starts by extending such datasets temporally (Sec. 3.1). Then we leverage these new bi-temporal pairs, along with the single-temporal annotations in order to train a semantic change detection model (Sec. 3.2). We detail our implementation in Sec. 3.3.

Problem Definition. Let \mathcal{D} be a single-temporal dataset of N aerial or satellite annotated images $I_{t_i}^i$ in $\mathbb{R}^{C \times H \times W}$ acquired at time t_i , for $i \in \{1, \dots, N\}$. C , H , and W respectively refer to the number of channels, height, and width of the images. Each $I_{t_i}^i$ is annotated with a semantic mask $S_{t_i}^i$ in $\{1, \dots, K\}^{H \times W}$, with K the number of semantic classes. Now, let f_θ be a deep neural network with learnable

parameters θ , returning, for a given input pair $(I_t, I_{t'})$ of bi-temporal images, a change map of pixels whose semantic class changes between the acquisition timestamps t and t' . Our goal is to train such a model f_θ , using the dataset \mathcal{D} extended with new, easily-available, non-annotated temporal acquisitions $I_{t'_i}$.

3.1. Data

To verify our methodology, we apply it to two existing aerial datasets, FLAIR [26] and the Inria aerial image labeling dataset (IAILD) [45], spanning areas in three countries (France, USA and Austria). Since we extend these datasets so they contain *bi-temporal* pairs, we prepend their name with “b-” to distinguish them from the original datasets.

b-FLAIR: FLAIR is based on aerial images from the French National Institute of Geographical and Forest Information (IGN)’s BD ORTHO [29]: a database of aerial orthophotographies covering the French territory at 0.2 meters per pixel (m/px). All 512×512 FLAIR image patches are annotated with semantic maps that assign each pixel to one of 19 land cover classes. BD ORTHO is renewed on average every three years, making it possible to collect aerial images of the same locations at different dates. We thus extract, for every FLAIR image, an additional observation from the BD ORTHO database at around three years before or after the original FLAIR acquisition. b-FLAIR is challenging for weakly supervised change detection with single-date annotations for two reasons. First, FLAIR areas were selected for land cover diversity with no particular temporal consideration, probably resulting in a low proportion of pairs with relevant semantic change. Second, approximately 30% of pairs have acquisition dates differing by two or more months, introducing seasonal variations that, combined with varying acquisition times within the day, may introduce significant radiometric and shadow changes.

b-IAILD: IAILD covers urban areas in the USA and Austria. We only extended IAILD’s training set, as its test set is not publicly available. It consists of 180 patches of size 5000×5000 at a resolution of 0.3 m/px, annotated with binary building footprint masks. For each location, we gathered a patch from the most recent available orthoimage acquisition campaign released by the corresponding agency (USGS for the USA, and the respective GIS agencies for Austrian provinces). The added images have acquisition dates spanning 2022 to 2024, while IAILD’s original images were acquired before 2017. Because the new acquisitions have spatial resolutions varying from 0.15 to 0.6 m/px, we standardized b-IAILD to 0.6 m/px. Due to IAILD’s urban focus, we expect b-IAILD to contain more examples of changes related to artificialization and building construction or demolition.

b-FLAIR-spot: To verify our methodology beyond very high resolution aerial imagery, we also created a satellite vari-

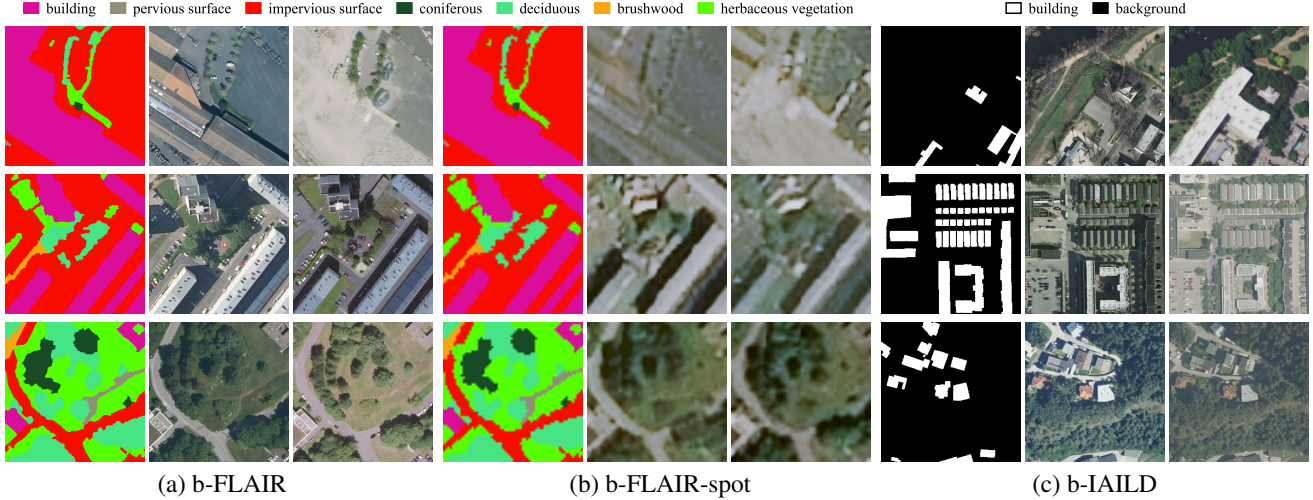


Figure 2. **Visual examples.** For each of the extended datasets, we show example triplets $(S_t, I_t, I_{t'})$ in this order from left to right, corresponding to the annotation mask, the original image, and the added acquisition respectively. Pairs may exhibit significant land cover changes (top row), or irrelevant changes due to shadows or seasonal variations (middle and bottom rows).

ant of b-FLAIR. For each bi-temporal pair, we downloaded the corresponding SPOT-6/7 images from IGN’s ORTHO-SAT database [31] for the same acquisition year and location. The images have a spatial resolution of 1.5 m/px, which we resampled to 1.6 m/px to obtain 64×64 patches. The corresponding single-date semantic maps were also resampled to the same resolution via nearest neighbor interpolation. We refer to this satellite dataset as b-FLAIR-spot.

b-FLAIR, b-IAILD and b-FLAIR-spot thus contain triplets $(S_t, I_t, I_{t'})$. We show example of such triplets in Fig. 2. Further details on these datasets, and additional example images can be found in the Supplementary Material.

Evaluation Datasets. We evaluate competing methods on 5 datasets. For the in-domain evaluation of methods trained on b-FLAIR and b-FLAIR-spot, we release b-FLAIR-test and b-FLAIR-test-spot, two evaluation sets of 1730 image pairs annotated with a binary building change mask. The images are in the same format as FLAIR images and were acquired, processed, and formatted following the procedure described in [25]. The images were extracted from 9 different French administrative departments and do not intersect the FLAIR dataset, which allows for a sound evaluation of methods trained on FLAIR or on our bi-temporal extensions of FLAIR. The pairs were annotated by photointerpretation experts and verified by a non-expert assessor. The pairs either show new building constructions, or no building change at all ($\sim 30\%$ of the pairs), and no pair exhibits building destruction. For the out-of-domain evaluation of all methods, we selected LEVIR-CD [14], WHU-CD [33], and S2Looking [54], three datasets commonly used in building change detection benchmarks. Hyperparameter studies are performed using a subset of b-FLAIR for training, and b-FLAIR-test for evaluation. More details on the evaluation

can be found in the Supplementary Material.

3.2. Training with single date labels

Given a set of triplets $(S_{t_i}^i, I_{t_i}^i, I_{t'_i}^i)_{i=1,\dots,N}$, our goal is to train a bi-temporal change detection neural network f_θ . Our methodology can be applied to any model predicting, for an input image pair $(I_t, I_{t'})$, a triplet $(\hat{S}_t, \hat{S}_{t'}, \hat{M})$ respectively consisting of a semantic mask for each frame and a binary change mask. A widely accepted architecture for semantic change detection indeed consists of a triple-branch network [13, 21, 23, 24, 69] with two semantic segmentation branches and a binary change branch. We now detail the three main components of our training strategy: balanced batch sampling, change map generation, and iterative refinement.

Balanced batch sampling. Our extended datasets typically contain a small fraction of pairs exhibiting actual change events. Zheng *et al.* [72] compensate the lack of annotated change datasets in the literature by artificially pairing images from different locations, using as change labels a difference of their respective semantic masks. Building on this idea, we choose to mix in a single batch such *fake* pairs with *real* bi-temporal pairs. We thus introduce a parameter p_{real} in $[0, 1]$, corresponding to the proportion of real pairs in each batch. Specifically, for a batch of size B of pairs $(I_{t_i}^i, I_{t'_i}^i)_{i=1,\dots,B}$ sampled from \mathcal{D} , the method splits it into N_{real} bi-temporal examples and N_{fake} unaligned examples, following:

$$N_{\text{real}} = \lfloor B \times p_{\text{real}} \rfloor, \quad N_{\text{fake}} = B - N_{\text{real}}. \quad (1)$$

We apply a random permutation to the N_{fake} samples, such that the image $I_{t_i}^i$ is paired with $I_{t'_j}^j$ with $j \neq i$.

Change map generation. The models trained with our method usually supervise their predicted maps $(\hat{S}_t, \hat{S}_{t'}, \hat{M})$

Table 1. **Comparison with baselines.** For each data source, the best-performing results are shown in **bold**. Second-best results are underlined. Note that SyntheWorld is a fully synthetic dataset, in contrast to FSC-180k, which is built on FLAIR; therefore, evaluation on real data is always out-of-domain for models trained on SyntheWorld. [†]Results from [4].

Data source	Model	Dataset extension	Bi-temporal				Post-classif.	Synthetic	STAR [72]	Ours	In-domain				Out-of-Domain							
			b-FLAIR-test		b-FLAIR-spot-test						LEVIR-CD		WHU-CD		S2Looking							
			F1	IoU	F1	IoU					F1	IoU	F1	IoU	F1	IoU						
FLAIR	UNet	—	✗	✓	✗	✗	✗	✗	62.6	45.5	—	—	31.9	19.0	62.0	44.9	12.1	6.5				
	UNet	b-FLAIR	✓	✓	✗	✗	✗	✗	65.2	48.3	—	—	35.3	21.4	65.2	48.3	12.5	6.7				
	Dual UNet	FSC-180k [4]	✗	✗	✓	✗	✗	✗	83.1	71.1	—	—	49 [†]	33 [†]	63.3	46.3	4 [†]	2 [†]				
	Dual UNet	—	✗	✗	✗	✓	✗	✗	75.9	61.1	—	—	37.5	23.1	70.6	54.5	13.7	7.4				
	Dual UNet	b-FLAIR	✓	✗	✗	✗	✓	✗	79.0	65.3	—	—	17.8	9.3	77.3	63.0	13.6	7.3				
FLAIR-spot	UNet	—	✗	✓	✗	✗	✗	✗	—	—	24.1	13.7	3.0	1.5	15.2	8.2	0.4	0.2				
	UNet	b-FLAIR-spot	✓	✓	✗	✗	✗	✗	—	—	25.0	14.3	19.5	10.8	28.6	16.7	1.9	1.0				
	Dual UNet	—	✗	✗	✗	✓	✗	✗	—	—	29.2	17.1	0.7	0.4	5.2	2.7	0.1	0				
	Dual UNet	b-FLAIR-spot	✓	✗	✗	✗	✗	✓	—	—	22.9	12.9	34.1	20.6	49.3	32.7	7.1	3.7				
IAILD	UNet	—	✗	✓	✗	✗	✗	✗	—	—	—	—	53.1	36.2	42.6	27.1	4.6	2.4				
	UNet	b-IAILD	✓	✓	✗	✗	✗	✗	—	—	—	—	44.9	28.9	44.5	28.6	7.9	4.1				
	Dual UNet	—	✗	✗	✗	✓	✗	✗	—	—	—	—	54.7	37.6	53.7	36.7	6.1	3.1				
	Dual UNet	b-IAILD	✓	✗	✗	✗	✗	✓	—	—	—	—	35.9	21.9	63.3	46.3	17.6	9.6				
	Dual UNet	SyntheWorld [56]	✗	✗	✓	✗	✗	✗	—	—	—	—	25 [†]	13 [†]	25.1	14.3	0 [†]	0 [†]				

with ground-truth maps $(S_t, S_{t'}, M)$. In our weakly supervised setting, we only have access to S_t . We create missing semantic and change maps distinguishing two cases, depending on if the pair is real or fake. For real pairs, we make the rough assumption that there is no semantically relevant change between the two acquisitions, and define:

$$S_{t'} = S_t, \quad M = 0. \quad (2)$$

For fake pairs $(I_{t_i}^i, I_{t_j}^j)$, we use the semantic mask of $I_{t_j}^j$ as proxy of the unavailable mask $I_{t_j}^j$, again assuming no change between the two acquisitions. In order to generate a change mask M from this pair of non-spatially aligned maps S_{t_i} and S_{t_j} , Zheng *et al.* [72] apply an XOR operation, which only consider the semantic temporal differences at the pixel level. Instead, we choose to use an object-aware metric that considers changes at the object level. To this end, we generate a change mask by thresholding the sIoU [12, 51] between connected components of S_{t_i} and S_{t_j} . The sIoU is a well-adopted object-level variation of the traditional intersection over union (IoU). Unlike the conventional IoU, which penalizes fragmented ground truth regions by assigning each prediction a moderate IoU score, the sIoU does not penalize predictions for a segmentation if other predicted segmentations sufficiently cover the remaining ground truth. This enables a robust evaluation of changes at the object level, especially when accounting for shadow occlusions, deformations, or label inconsistencies. Let \mathcal{C}_{t_i} and \mathcal{C}_{t_j} denote the sets of connected components in S_{t_i} and S_{t_j} respectively, where each component corresponds to a semantic class. We compute the sIoU between each component c^k in \mathcal{C}_{t_i} , characterized by its semantic category k , with respect to \mathcal{C}_{t_j}

as

$$\text{sIoU}_{\mathcal{C}_{t_j}}(c^k) := \frac{|\mathcal{C}_{t_j}(c^k)|}{|(\mathcal{C}_{t_j} \cup \mathcal{C}_{t_j}(c^k)) \setminus \mathcal{A}(c^k)|}, \quad (3)$$

with

$$\mathcal{C}_{t_j}(c^k) = \bigcup_{\bar{c}^l \in \mathcal{C}_{t_j}} \bar{c}^l \text{ and } \mathcal{A}(c^k) = \bigcup_{\substack{\bar{c}^l \in \mathcal{C}_{t_i} \setminus \{c^k\} \\ \bar{c}^l \cap c^k \neq \emptyset, l=k}} \bar{c}^l. \quad (4)$$

The notation $|\cdot|$ denotes the size of a set in terms of number of pixels. The term $\mathcal{A}(c^k)$ excludes from the denominator any pixels belonging to other \mathcal{C}_{t_i} components that overlap with c^k and share the same semantic class k , preventing interference from nearby objects. During training, we apply this object-level comparison to each fake pair in the batch. For each pair of semantic maps (S_{t_i}, S_{t_j}) , we compute the sIoU for all components in both directions: \mathcal{C}_{t_i} with respect to \mathcal{C}_{t_j} , and vice versa. A pixel location (x, y) of the binary change mask M is labeled as a change if it belongs to any connected component in either \mathcal{C}_{t_i} or \mathcal{C}_{t_j} for which the sIoU is below a predefined threshold τ :

$$M(x, y) = \begin{cases} 1 & \text{if } (x, y) \in \bigcup_{\substack{c \in \mathcal{C}_{t_i} \\ \text{sIoU}_{\mathcal{C}_{t_j}}(c) < \tau}} c, \\ 1 & \text{if } (x, y) \in \bigcup_{\substack{c \in \mathcal{C}_{t_j} \\ \text{sIoU}_{\mathcal{C}_{t_i}}(c) < \tau}} c, \\ 0 & \text{otherwise.} \end{cases} \quad (5)$$

Fig. 3 provides a visual explanation of the motivations and effects of the object-level change map generation based on

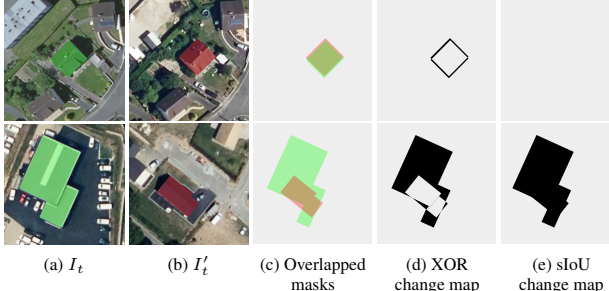


Figure 3. **XOR vs. sIoU for change map generation** from image pairs, for the building change detection binary task. Top: a real pair with slight viewpoint variation—XOR falsely detects changes, while sIoU correctly shows none. Bottom: a *fake* pair with different buildings—XOR misses overlapping changes, sIoU correctly marks both. Only one building per image is labeled for clarity.

the sIoU. In particular, our method is consistent with labeling co-registered real pairs with zero change maps, whereas XOR change maps are sensitive to viewpoint changes.

Iterative refinement. The rough assumption that real bi-temporal pairs can be labeled with a zero change mask introduces noise in the supervision signal. Indeed, genuine semantic changes may have occurred during the several years separating the original and new acquisitions added in our extended datasets. This leads to mislabeled training samples where changes are incorrectly treated as unchanged, which can degrade model performance. To mitigate this, we adopt an iterative refinement strategy. First, we train a model on the entire dataset. We then use its predictions to identify and filter out image pairs likely to contain changes. In practice, we remove all image pairs for which the model predicts more than 2% of changed pixels. In the next iteration, we train a model from scratch using this cleaned dataset, therefore improving training stability and overall prediction quality. We repeat this for N_{iter} iterations, where N_{iter} is a hyperparameter of the method. Ignoring a subset of the dataset by removing noisy or incorrect samples, also known as data cleaning, has been proven successful in other works [19, 27, 32, 35].

3.3. Implementation

Recent analyses show that simple baselines like UNet remain highly competitive for change detection despite the proliferation of complex task-specific architectures [18]. As architectural design is beyond the scope of this paper, we adopt a 3-branch Dual UNet, following Benidir *et al* [4]. Note that the proposed methodology is architecture agnostic and as such can also be applied to any 3-branch models.

We train our models in a multi-task setting, supervising the semantic segmentation at both dates as well as the binary change detection with corresponding focal losses. All models are trained using the AdamW optimizer [44] with

a 1e-2 weight decay over 100 epochs and a learning rate of 1e-4. We keep the model with the best validation IoU on the segmentation task over the original sample t . We only use the RGB bands of the images in the datasets, and focus on building change detection when not explicitly stated otherwise. For example, with FLAIR-based datasets, we ignore infrared and elevation bands, merging all non-building classes into a “background” class. Our hyperparameters are set to $p_{\text{real}} = 0.25$, $\tau = 0.25$, and $N_{\text{iter}} = 3$.

4. Experiments

Baselines. We compare our methodology with four frameworks that use single-temporal semantic segmentation annotations for change detection. These include post-classification with and without multi-temporal data augmentation, synthetic dataset learning, and STAR [72], which generates *fake change pairs* by pairing images from different locations in single-temporal datasets. For post-classification, we train a UNet [50] on the semantic segmentation task and detect building changes by comparing bi-temporal predictions. Bi-temporal data augmentation is achieved by using our extended data during training. Lastly, we consider two Dual UNet [4] frameworks trained on synthetic datasets: SyntheWorld [56] and FSC-180k [4].

Metrics. We adopt F1-score (F1) and intersection over union (IoU) as evaluation metrics for building change detection. These scores are reported as percentages. We also report the false positive rates (FPR), and the number and size of connected components to evaluate false alarms.

In-domain results. Tab. 1 reports in-domain performance on the b-FLAIR-test and b-FLAIR-test-spot datasets (described in Sec. 3.1), with qualitative examples in Fig. 4. Our method achieves the second-best score on b-FLAIR-test, while performance slightly drops on b-FLAIR-test-spot. We attribute this to two main factors. (1) Our weak supervision relies on temporal augmentation, which can introduce minor misalignments or imperfect change annotations. This produces slightly *dilated* predictions, smoother boundaries and less defined corners, affecting IoU and F1 scores. (2) The model assumes most regions remain unchanged between acquisitions, biasing predictions toward the no-change class. Given change detection datasets are dominated by the background class, false negatives penalize IoU and F1 more than false positives.

Beyond quantitative results, Fig. 4 confirms that our model is notably more robust in no-change regions, producing fewer false positives. We argue that this behavior is desirable: in large-scale deployments, minimizing false alarms is often more critical than achieving perfectly sharp change boundaries. Therefore, we complement our evaluation with an analysis of the FPR and connected components. Tab. 2 reports FPR, number of change connected components per

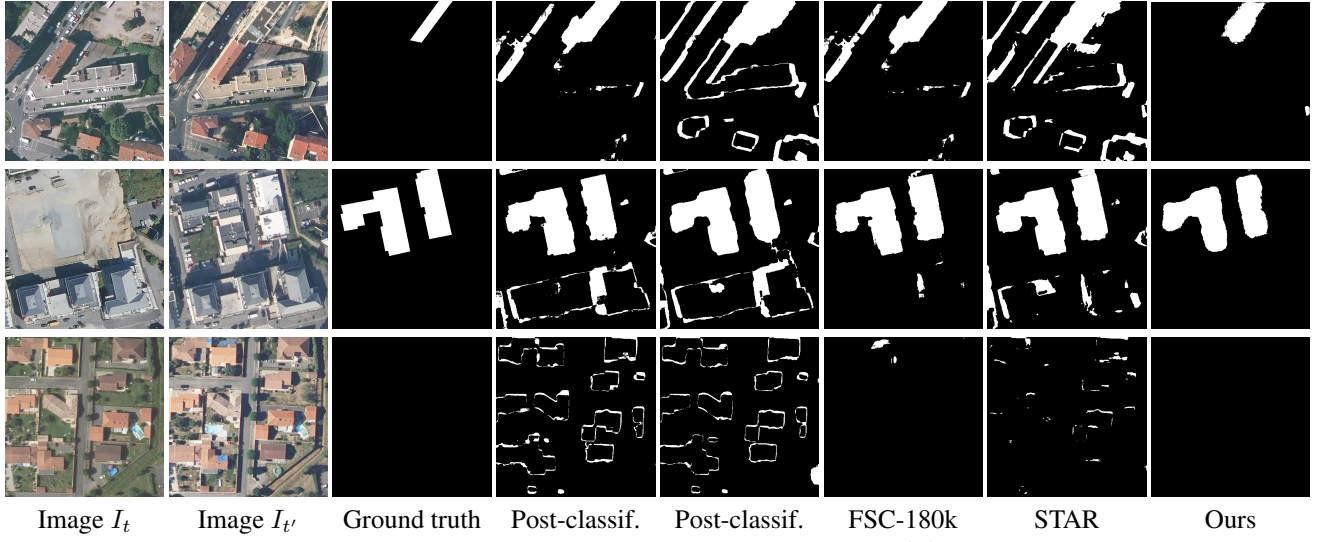


Figure 4. **Qualitative results on b-FLAIR-test.** We compare the building change maps predicted by baseline methods and ours.

Table 2. **Comparison between our method and a pretraining on FSC-180k** [4] on b-FLAIR-test. We report the false positive rate (FPR) of both methods, as well as object-related indicators: average number of change objects per pair, and average size of change objects. An object is defined as a pixel-connected component in the binary building change map.

	5x5 median filter	FPR (↓)	Num. obj. (avg)	Obj. size (avg, m ²)
Ground truth	—	—	1.7	187
FSC-180k pretraining [4]	✗	0.73	12.1	30
Ours (b-FLAIR)	✗	0.35	3.0	87
FSC-180k pretraining [4]	✓	0.71	3.6	98
Ours (b-FLAIR)	✓	0.28	1.8	145

image pair, and average component size for our predictions, ground truth, and those of Benidir *et al.* [4]. Component-level evaluation treats small isolated pixels equally to large false detections. While such small artifacts can be easily removed through simple post-processing, larger false detections are more challenging to handle. Following prior work [6, 8, 49], we report results both before and after applying a 5×5 median filter on the change maps. Across both metrics, our model produces substantially fewer false positives, consistent with the qualitative large-scale results in Fig. 1, where our predictions closely align with ground truth while FSC-180k shows numerous false alarms.

Out-of-domain results. We further evaluate zero-shot building change detection performance on LEVIR-CD, WHU-CD, and S2Looking, as reported in Tab. 1. Comparisons are made across models trained on the same data sources (FLAIR, SPOT, and IAILD), with the best results highlighted for each setting. Our method achieves the best overall performance on WHU-CD and S2Looking, and consistently outperforms direct competitors within each training domain.

Table 3. **Low data regime results.** IoU scores on LEVIR-CD and S2Looking datasets when fine-tuning a Dual UNet on limited target data (1%, 10% and 30%). Each result is averaged over 10 runs. Bold values denote the best performance for each dataset. [†]Results from [4].

Pretraining dataset	Proportion of target data used		
	1%	10%	30%
LEVIR-CD			
No pre-training [†]	0.36	0.69	0.75
SyntheWorld [†]	0.41 (+14%)	0.71 (+3%)	0.77 (+3%)
FSC-180k [†]	0.55 (+53%)	0.73 (+6%)	0.79 (+5%)
b-FLAIR	0.60 (+67%)	0.77 (+12%)	0.81 (+8%)
b-IAILD	0.67 (+86%)	0.79 (+14%)	0.82 (+9%)
S2Looking			
No pre-training [†]	0.10	0.27	0.38
SyntheWorld [†]	0.08 (-20%)	0.34 (+26%)	0.41 (+8%)
FSC-180k [†]	0.15 (+50%)	0.36 (+33%)	0.43 (+13%)
b-FLAIR	0.24 (+140%)	0.31 (+15%)	0.41 (+8%)
b-IAILD	0.27 (+170%)	0.37 (+37%)	0.41 (+8%)

The only exception is the b-FLAIR variant on S2Looking, which ranks second by a marginal difference. On LEVIR-CD, the b-FLAIR-spot model surpasses its counterparts, although the b-FLAIR and b-IAILD variants report lower performances. We also point out that these datasets are “very” out-of-domain for models trained using FLAIR-spot because of the difference in resolution ($\sim 1.6\text{m}$ vs $\sim 20\text{cm}$).

Results in low-data regime. We finetune a Dual UNet, pre-trained with our methodology, on small subsets of 1%, 10%, and 30% of training data for LEVIR-CD and S2Looking. This evaluates the quality of the learned representations when training with very few samples, a common practical

Table 4. **Impact of p_{real} and τ .** Left: Comparison of different values for the proportion p_{real} of real bi-temporal pairs in training batches. Right: Comparison between XOR change maps and our sIoU-based change maps computed with different threshold τ . Scores reported on b-FLAIR-test.

p_{real}	F1	IoU	XOR	sIoU	τ	F1	IoU
0.00	72.3	56.6	✓		—	76.0	61.3
0.10	76.1	61.4	✓	0.75	74.8	59.7	
0.25	77.0	62.6	✓	0.50	73.1	57.8	
0.35	73.8	58.5	✓	0.25	77.0	62.6	
0.50	73.6	58.2					

Table 5. **Performance across training iterations.** F1 Score (%) and IoU (%) of a Dual UNet trained with our method over three training iterations, and evaluated on the corresponding in-domain test set. Best results per dataset are shown in bold.

	b-FLAIR		b-FLAIR-spot	
	F1	IoU	F1	IoU
Iteration 1	67.3	50.7	22.6	12.7
Iteration 2	78.1	64.1	21.7	12.2
Iteration 3	79.0	65.2	22.9	12.9

scenario. Following the protocol of Benidir *et al.* [4], we randomly sample training sets from the target dataset and average results over 10 runs. Tab. 3 reports results for our b-FLAIR and b-IAILD models, compared with FSC-180k and SyntheWorld from [4]. Our approach achieves substantial improvements over the state of the art when only minimal annotations are available (e.g., 1%), while performance converges as more data is available.

4.1. Hyperparameters analysis

For the hyperparameters τ and p_{real} , we report the scores of models trained on a subset of b-FLAIR.

Impact of p_{real} . Tab. 4 shows adding real pairs in a batch improves performance, with $p_{\text{real}} = 0$ yielding the lowest scores. Performance peaks at $p_{\text{real}} = 0.25$, while higher values degrade it, likely because overrepresented real pairs with no change bias the model toward predicting no change.

Impact of τ . As shown in Tab. 4, a threshold of $\tau = 0.25$ for sIoU-based change map generation outperforms the logical XOR operation. On the contrary, higher thresholds ($\tau \in \{0.5, 0.75\}$) tend to classify components as changed despite significant overlap between building footprints across the two masks, resulting in noisy supervision. Note that $\tau = 1$ reduces our sIoU-based maps to the OR operation, which Zheng *et al.* [76] demonstrated to be inferior to XOR-based change maps for training change detection models. Visualizations comparing these different change map generation variants are provided in the Supplementary Material.

Impact of the iterative refinement. Our methodology relies on mixing bi-temporal image pairs with fake pairs of

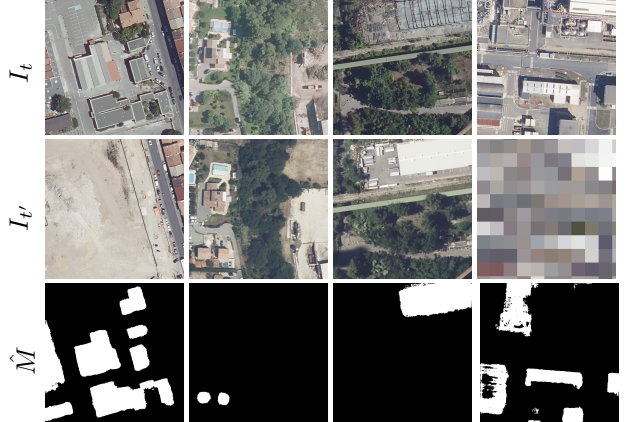


Figure 5. **Samples removed during iterative refinement.** Triplets (I_t , $I_{t'}$, \hat{M}) removed during refinement exhibit real building changes or blurred sensitive areas, where the assumption $M = 0$ does not hold. Such samples are correctly identified by the model and excluded from the training set on subsequent iterations.

unaligned images, while assuming by default that all real pairs contain no change. This assumption is incorrect in practice in certain cases, particularly since our extension of existing single-temporal datasets is based on new acquisitions often captured several years apart. Tab. 5 therefore demonstrates the benefit of iterative cleaning of the extended datasets, through filtering of image pairs that would contain significant semantic changes. For b-FLAIR, the second iteration increases F1 by over 10pt and IoU by nearly 14pt on b-FLAIR-test, while gains at the third iteration are smaller. We therefore set $N_{\text{iter}} = 3$ by default. Fig. 5 illustrates filtered pairs, including building changes and blurred sensitive areas. On b-FLAIR-spot, successive iterations have little effect.

5. Conclusion

In this article, we introduced a novel approach for training remote sensing change detection models by extending single-date datasets and supervising changes through weak temporal supervision, without additional annotations. We assume no change occurs between two observations of the same location while providing change examples by pairing images from different locations. Extensive experiments across multiple datasets show that our methodology learns models with strong out-of-distribution generalization, can be fine-tuned with minimal annotations, and are robust to false positives in “in the wild” scenarios. Qualitative results demonstrate strong alignment with ground truth building construction and demolition maps, bridging the gap between weak supervision and reliable large-scale change monitoring. Overall, our framework offers a practical, annotation-efficient approach to scalable change detection for both aerial and remote sensing observations.

Acknowledgement

This work was funded by AID-DGA (l’Agence de l’Innovation de Défense à la Direction Générale de l’Armement—Ministère des Armées), and was performed using HPC resources from GENCI-IDRIS (grants 2023-AD011011801R3, 2023-AD011012453R2, 2023-AD011012458R2) and from the “Mésocentre” computing center of CentraleSupélec and ENS Paris-Saclay supported by CNRS and Région Île-de-France (<http://mesocentre.universite-paris-saclay.fr>). Centre Borelli is also with Université Paris Cité, SSA and INSERM. This work is additionally supported by RGC-GRF project 11309925, Mathematical Formalization of GIS. We thank Etienne Bourgeat, Fabien Poilane and Floryne Roche for their valuable assistance in data curation and annotation.

References

- [1] Philipp Andermatt and Radu Timofte. A weakly supervised convolutional network for change segmentation and classification. In *Proceedings of the Asian conference on computer vision*, 2020. [2](#)
- [2] Anju Asokan and JGESI Anitha. Change detection techniques for remote sensing applications: A survey. *Earth Science Informatics*, 12(2):143–160, 2019. [2](#)
- [3] Christian Ayala, C Aranda, and Mikel Galar. Multi-temporal data augmentation for high frequency satellite imagery: A case study in sentinel-1 and sentinel-2 building and road segmentation. *The International Archives of the Photogrammetry, Remote Sensing and Spatial Information Sciences*, 43:25–32, 2022. [3](#)
- [4] Yanis Benidir, Nicolas Gonthier, and Clément Mallet. The change you want to detect: Semantic change detection in earth observation with hybrid data generationf. In *Proceedings of the Computer Vision and Pattern Recognition Conference*, pages 2204–2214, 2025. [1, 2, 3, 5, 6, 7, 8, 4](#)
- [5] Xavier Bou, Thibaud Ehret, Rafael Grompone Von Gioi, and Jérémie Anger. Portraying the need for temporal data in flood detection via sentinel-1. In *IGARSS 2024-2024 IEEE International Geoscience and Remote Sensing Symposium*, pages 3930–3934. IEEE, 2024. [2](#)
- [6] Xavier Bou, Aitor Artola, Thibaud Ehret, Gabriele Facciolo, Jean-Michel Morel, and Rafael Grompone von Gioi. Statistical modeling of deep features to reduce false alarms in video change detection. *Journal of Mathematical Imaging and Vision*, 67(2):19, 2025. [7](#)
- [7] Dominik Brunner, Lorenzo Bruzzone, and Guido Lemoine. Change detection for earthquake damage assessment in built-up areas using very high resolution optical and sar imagery. In *2010 IEEE international geoscience and remote sensing symposium*, pages 3210–3213. IEEE, 2010. [2](#)
- [8] Sebastian Brutzer, Benjamin Höferlin, and Gunther Heidemann. Evaluation of background subtraction techniques for video surveillance. In *CVPR 2011*, pages 1937–1944, 2011. [7](#)
- [9] Yinxia Cao and Xin Huang. A full-level fused cross-task transfer learning method for building change detection using noise-robust pretrained networks on crowdsourced labels. *Remote Sensing of Environment*, 284:113371, 2023. [3](#)
- [10] R. Caye Daudt, B. Le Saux, A. Boulch, and Y. Gousseau. Urban change detection for multispectral earth observation using convolutional neural networks. In *IEEE International Geoscience and Remote Sensing Symposium (IGARSS)*, 2018. [2](#)
- [11] Turgay Celik. Unsupervised change detection in satellite images using principal component analysis and k -means clustering. *IEEE geoscience and remote sensing letters*, 6(4):772–776, 2009. [2](#)
- [12] Robin Chan, Krzysztof Lis, Svenja Uhlemeyer, Hermann Blum, Sina Honari, Roland Siegwart, Pascal Fua, Mathieu Salzmann, and Matthias Rottmann. Segmentmeifyoucan: A benchmark for anomaly segmentation. In *Proceedings of the Neural Information Processing Systems Track on Datasets and Benchmarks*, 2021. [2, 5](#)
- [13] Hao Chang, Peijin Wang, Wenhui Diao, Guangluan Xu, and Xian Sun. A triple-branch hybrid attention network with bitemporal feature joint refinement for remote-sensing image semantic change detection. *IEEE Transactions on Geoscience and Remote Sensing*, 62:1–16, 2024. [4](#)
- [14] Hao Chen and Zhenwei Shi. A spatial-temporal attention-based method and a new dataset for remote sensing image change detection. *Remote sensing*, 12(10):1662, 2020. [2, 4, 5](#)
- [15] Hongruixuan Chen, Jian Song, Chengxi Han, Junshi Xia, and Naoto Yokoya. Changemamba: Remote sensing change detection with spatiotemporal state space model. *IEEE Transactions on Geoscience and Remote Sensing*, 62:1–20, 2024. [2](#)
- [16] Guangliang Cheng, Yumeng Huang, Xiangtai Li, Shuchang Lyu, Zhaoyang Xu, Hongbo Zhao, Qi Zhao, and Shiming Xiang. Change detection methods for remote sensing in the last decade: A comprehensive review. *Remote Sensing*, 16(13):2355, 2024. [2](#)
- [17] Emilio Chuvieco, Inmaculada Aguado, Javier Salas, Mariano García, Marta Yebra, and Patricia Oliva. Satellite remote sensing contributions to wildland fire science and management. *Current Forestry Reports*, 6(2):81–96, 2020. [2](#)
- [18] Isaac Corley, Caleb Robinson, and Anthony Ortiz. A change detection reality check. In *International Conference on Learning Representations*, 2024. [6](#)
- [19] Pierre-Olivier Côté, Amin Nikanjam, Nafisa Ahmed, Dmytro Humeniuk, and Foutse Khomh. Data cleaning and machine learning: a systematic literature review. *Automated Software Engineering*, 31(2):54, 2024. [6](#)
- [20] Fengzhi Cui and Jie Jiang. Mtscd-net: A network based on multi-task learning for semantic change detection of bitemporal remote sensing images. *International Journal of Applied Earth Observation and Geoinformation*, 118:103294, 2023. [2](#)
- [21] Rodrigo Caye Daudt, Bertrand Le Saux, Alexandre Boulch, and Yann Gousseau. Multitask learning for large-scale semantic change detection. *Computer Vision and Image Understanding*, 187:102783, 2019. [2, 4](#)
- [22] Rodrigo Caye Daudt, Bertrand Le Saux, Alexandre Boulch, and Yann Gousseau. Weakly supervised change detection

using guided anisotropic diffusion. *Machine Learning*, 112(6):2211–2237, 2023. 3

[23] Lei Ding, Haitao Guo, Sicong Liu, Lichao Mou, Jing Zhang, and Lorenzo Bruzzone. Bi-temporal semantic reasoning for the semantic change detection in hr remote sensing images. *IEEE Transactions on Geoscience and Remote Sensing*, 60:1–14, 2022. 2, 4

[24] Lei Ding, Jing Zhang, Haitao Guo, Kai Zhang, Bing Liu, and Lorenzo Bruzzone. Joint spatio-temporal modeling for semantic change detection in remote sensing images. *IEEE Transactions on Geoscience and Remote Sensing*, 62:1–14, 2024. 2, 4, 5

[25] Anatol Garioud, Stéphane Peillet, Eva Bookjans, Sébastien Giordano, and Boris Wattrelot. Flair# 1: semantic segmentation and domain adaptation dataset. *arXiv preprint arXiv:2211.12979*, 2022. 4, 2, 3

[26] Anatol Garioud, Nicolas Gonthier, Loïc Landrieu, Apolline De Wit, Marion Valette, Marc Poupée, Sébastien Giordano, et al. Flair: a country-scale land cover semantic segmentation dataset from multi-source optical imagery. *Advances in Neural Information Processing Systems*, 36:16456–16482, 2023. 2, 3

[27] I Guyon, N Matić, and V Vapnik. Discovering informative patterns and data cleaning. In *Proceedings of the 3rd International Conference on Knowledge Discovery and Data Mining*, pages 145–156, 1994. 6

[28] Ibrahim Rizk Hegazy and Mosbeh Rashed Kaloop. Monitoring urban growth and land use change detection with gis and remote sensing techniques in daqahlia governorate egypt. *International journal of sustainable built environment*, 4(1):117–124, 2015. 2

[29] IGN - Institut national de l'information géographique et forestière. BD ORTHO®: L'image géographique du territoire national, la France vue du ciel. <https://geoservices.ign.fr/bdortho>, 2025. Accessed: October 21, 2025. 1, 2, 3, 5

[30] IGN - Institut national de l'information géographique et forestière. OCS GE : Un référentiel national utilisable aux différents échelons territoriaux pour la mise en place des politiques publiques d'aménagement du territoire et l'élaboration des documents d'urbanisme. <https://geoservices.ign.fr/ocsg>, 2025. Accessed: November 13, 2025. 1

[31] IGN - Institut national de l'information géographique et forestière. ORTHO-SAT®: Les ortho-images issues de prises de vues satellitaires. <https://geoservices.ign.fr/ortho-sat>, 2025. Accessed: October 21, 2025. 4, 2, 5

[32] Piyasak Jeatrakul, Kok Wai Wong, and Chun Che Fung. Data cleaning for classification using misclassification analysis. *Journal of Advanced Computational Intelligence and Intelligent Informatics*, 14(3):297–302, 2010. 6

[33] Shuping Ji, Shiqing Wei, and Meng Lu. Fully convolutional networks for multisource building extraction from an open aerial and satellite imagery data set. *IEEE Transactions on geoscience and remote sensing*, 57(1):574–586, 2018. 2, 4, 5

[34] Liangcun Jiang, Feng Li, Li Huang, Feifei Peng, and Lei Hu. Ttnet: A temporal-transform network for semantic change detection based on bi-temporal remote sensing images. *Remote Sensing*, 15(18):4555, 2023. 2

[35] George H John. Robust decision trees: Removing outliers from databases. In *KDD*, pages 174–179, 1995. 6

[36] Indrajit Kalita, Savvas Karatsiolis, and Andreas Kamilaris. Land use change detection using deep siamese neural networks and weakly supervised learning. In *International Conference on Computer Analysis of Images and Patterns*, pages 24–35. Springer, 2021. 2

[37] Salman H Khan, Xuming He, Fatih Porikli, and Mohammed Bennamoun. Forest change detection in incomplete satellite images with deep neural networks. *IEEE Transactions on Geoscience and Remote Sensing*, 55(9):5407–5423, 2017. 2

[38] Lazhar Khelifi and Max Mignotte. Deep learning for change detection in remote sensing images: Comprehensive review and meta-analysis. *Ieee Access*, 8:126385–126400, 2020. 2

[39] Zhuohong Li, Fangxiao Lu, Hongyan Zhang, Lilin Tu, Jiayi Li, Xin Huang, Caleb Robinson, Nikolay Malkin, Nebojsa Jojic, Pedram Ghamisi, et al. The outcome of the 2021 ieee grss data fusion contest—track msd: Multitemporal semantic change detection. *IEEE Journal of Selected Topics in Applied Earth Observations and Remote Sensing*, 15:1643–1655, 2022. 3

[40] Zhenglai Li, Chang Tang, Xinwang Liu, Wei Zhang, Jie Dou, Lizhe Wang, and Albert Y Zomaya. Lightweight remote sensing change detection with progressive feature aggregation and supervised attention. *IEEE Transactions on Geoscience and Remote Sensing*, 61:1–12, 2023. 2, 4, 5

[41] Fang Liu, Kanghua Yin, Jia Liu, Jingxiang Yang, Xu Tang, and Liang Xiao. Box2change: A novel weakly-supervised way for change detection via consistency instance segmentation. *IEEE Transactions on Geoscience and Remote Sensing*, 2025. 3

[42] Xuanguang Liu, Chengguang Dai, Zhenchao Zhang, Mengmeng Li, Hanyun Wang, Hongliang Ji, and Yujie Li. Tbscdnet: A siamese multi-task network integrating transformers and boundary regularization for semantic change detection from vhr satellite images. *IEEE Geoscience and Remote Sensing Letters*, 2024. 2

[43] Jiang Long, Sicong Liu, Mengmeng Li, Hang Zhao, and Yanmin Jin. Bgsnet: A boundary-guided siamese multitask network for semantic change detection from high-resolution remote sensing images. *ISPRS Journal of Photogrammetry and Remote Sensing*, 225:221–237, 2025. 2

[44] Ilya Loshchilov and Frank Hutter. Decoupled weight decay regularization. In *International Conference on Learning Representations*, 2019. 6

[45] Emmanuel Maggiore, Yuliya Tarabalka, Guillaume Charpiat, and Pierre Alliez. Can semantic labeling methods generalize to any city? the inria aerial image labeling benchmark. In *IEEE International Geoscience and Remote Sensing Symposium (IGARSS)*. IEEE, 2017. 2, 3

[46] National Aeronautics and Space Administration. Landsat timeline of satellites. <https://landsat.gsfc.nasa.gov/satellites/timeline>, 2024. Accessed: November 05, 2025. 2

[47] Hyeoncheol Noh, Jingi Ju, Minseok Seo, Jongchan Park, and Dong-Geol Choi. Unsupervised change detection based on image reconstruction loss. In *proceedings of the IEEE/CVF*

conference on computer vision and pattern recognition, pages 1352–1361, 2022. 2

[48] Jay N Paranjape, Celso De Melo, and Vishal M Patel. A mamba-based siamese network for remote sensing change detection. In *2025 IEEE/CVF Winter Conference on Applications of Computer Vision (WACV)*, pages 1186–1196. IEEE, 2025. 2

[49] Donovan H Parks and Sidney S Fels. Evaluation of background subtraction algorithms with post-processing. In *2008 IEEE fifth international conference on advanced video and signal based surveillance*, pages 192–199. IEEE, 2008. 7

[50] Olaf Ronneberger, Philipp Fischer, and Thomas Brox. U-net: Convolutional networks for biomedical image segmentation. In *International Conference on Medical image computing and computer-assisted intervention*, pages 234–241. Springer, 2015. 6

[51] Matthias Rottmann, Pascal Colling, Thomas Paul Hack, Robin Chan, Fabian Hüger, Peter Schlicht, and Hanno Gottschalk. Prediction error meta classification in semantic segmentation: Detection via aggregated dispersion measures of softmax probabilities. In *2020 International Joint Conference on Neural Networks (IJCNN)*, pages 1–9. IEEE, 2020. 2, 5

[52] Minseok Seo, Hakjin Lee, Yongjin Jeon, and Junghoon Seo. Self-pair: Synthesizing changes from single source for object change detection in remote sensing imagery. In *Proceedings of the IEEE/CVF Winter Conference on Applications of Computer Vision*, pages 6374–6383, 2023. 2, 3

[53] Ayesha Shafique, Guo Cao, Zia Khan, Muhammad Asad, and Muhammad Aslam. Deep learning-based change detection in remote sensing images: A review. *Remote Sensing*, 14(4):871, 2022. 2

[54] Li Shen, Yao Lu, Hao Chen, Hao Wei, Donghai Xie, Jiabao Yue, Rui Chen, Shouye Lv, and Bitao Jiang. S2looking: A satellite side-looking dataset for building change detection. *Remote Sensing*, 13(24):5094, 2021. 2, 4, 5

[55] Ashbindu Singh. Review article digital change detection techniques using remotely-sensed data. *International journal of remote sensing*, 10(6):989–1003, 1989. 3

[56] Jian Song, Hongruixuan Chen, and Naoto Yokoya. Syntheworld: A large-scale synthetic dataset for land cover mapping and building change detection. In *Proceedings of the IEEE/CVF Winter Conference on Applications of Computer Vision*, pages 8287–8296, 2024. 5, 6, 7

[57] Xiaoliang Tan, Guanzhou Chen, Xiaodong Zhang, Tong Wang, Jiaqi Wang, Kui Wang, and Tingxuan Miao. Triples: Mitigating multi-task learning conflicts for semantic change detection in high-resolution remote sensing imagery. *ISPRS Journal of Photogrammetry and Remote Sensing*, 230:374–401, 2025. 2

[58] Kai Tang and Jin Chen. Changeanywhere: Sample generation for remote sensing change detection via semantic latent diffusion model. *arXiv preprint arXiv:2404.08892*, 2024. 3

[59] Andrew P Tewkesbury, Alexis J Comber, Nicholas J Tate, Alistair Lamb, and Peter F Fisher. A critical synthesis of remotely sensed optical image change detection techniques. *Remote Sensing of Environment*, 160:1–14, 2015. 3

[60] The European Spatial Agency. Sentinel-2 operations. https://www.esa.int/Enabling_Support/Operations/Sentinel-2_operations, 2017. Accessed: November 05, 2025. 2

[61] Shiqi Tian, Yanfei Zhong, Zhuo Zheng, Ailong Ma, Xicheng Tan, and Liangpei Zhang. Large-scale deep learning based binary and semantic change detection in ultra high resolution remote sensing imagery: From benchmark datasets to urban application. *ISPRS Journal of Photogrammetry and Remote Sensing*, 193:164–186, 2022. 2

[62] Aysim Toker, Lukas Kondmann, Mark Weber, Marvin Eisenberger, Andrés Camero, Jingliang Hu, Ariadna Pregel Hodrelein, Çağlar Şenaras, Timothy Davis, Daniel Cremers, et al. Dynamicearthnet: Daily multi-spectral satellite dataset for semantic change segmentation. In *Proceedings of the IEEE/CVF Conference on Computer Vision and Pattern Recognition*, pages 21158–21167, 2022. 3

[63] U.S. Geological Survey. How often is orthoimagery in The National Map updated and what are the acquisition dates? <https://www.usgs.gov/faqs/how-often-orthoimagery-national-map-updated-and-what-are-acquisition-dates>, 2022. Accessed: November 05, 2025. 2

[64] Jiahao Wang, Fang Liu, Hao Wang, Xu Liu, Licheng Jiao, Hua Yang, Lingling Li, and Puhua Chen. Sdcenet: A semi-dual change detection network framework with super-weak label for remote sensing image. *IEEE Transactions on Geoscience and Remote Sensing*, 61:1–14, 2023. 3

[65] Lukang Wang, Min Zhang, and Wenzhong Shi. Cs-wscdnet: Class activation mapping and segment anything model-based framework for weakly supervised change detection. *IEEE Transactions on Geoscience and Remote Sensing*, 61:1–12, 2023. 2

[66] Manabu Watanabe, Christian N Koyama, Masato Hayashi, Izumi Nagatani, and Masanobu Shimada. Early-stage deforestation detection in the tropics with l-band sar. *IEEE journal of selected topics in applied earth observations and remote sensing*, 11(6):2127–2133, 2018. 2

[67] Qingke Wen, Zengxiang Zhang, Lifeng Shi, Xiaoli Zhao, Fang Liu, Jinyong Xu, Ling Yi, Bin Liu, Xiao Wang, Lijun Zuo, et al. Extraction of basic trends of urban expansion in china over past 40 years from satellite images. *Chinese Geographical Science*, 26(2):129–142, 2016. 2

[68] Hao Xia, Yugang Tian, Lihao Zhang, and Shuangliang Li. A deep siamese postclassification fusion network for semantic change detection. *IEEE Transactions on Geoscience and Remote Sensing*, 60:1–16, 2022. 2

[69] Kunping Yang, Gui-Song Xia, Zicheng Liu, Bo Du, Wen Yang, Marcello Pelillo, and Liangpei Zhang. Asymmetric siamese networks for semantic change detection in aerial images. *IEEE Transactions on Geoscience and Remote Sensing*, 60:1–18, 2021. 2, 4

[70] Manqi Zhao, Zifei Zhao, Shuai Gong, Yunfei Liu, Jian Yang, Xiong Xiong, and Shengyang Li. Spatially and semantically enhanced siamese network for semantic change detection in high-resolution remote sensing images. *IEEE Journal of Selected Topics in Applied Earth Observations and Remote Sensing*, 15:2563–2573, 2022. 2

- [71] Daoyuan Zheng, Shaohua Wang, Haixia Feng, Rui Xu, Shunli Wang, Mingyao Ai, Pengcheng Zhao, and Qingwu Hu. Csnet: Change selection of activations and pseudomasks for image-level weakly supervised change detection. *IEEE Transactions on Geoscience and Remote Sensing*, 2025. 2
- [72] Zhuo Zheng, Ailong Ma, Liangpei Zhang, and Yanfei Zhong. Change is everywhere: Single-temporal supervised object change detection in remote sensing imagery. In *Proceedings of the IEEE/CVF international conference on computer vision*, pages 15193–15202, 2021. 2, 3, 4, 5, 6, 8
- [73] Zhuo Zheng, Yanfei Zhong, Shiqi Tian, Ailong Ma, and Liangpei Zhang. Changemask: Deep multi-task encoder-transformer-decoder architecture for semantic change detection. *ISPRS Journal of Photogrammetry and Remote Sensing*, 183:228–239, 2022. 2
- [74] Zhuo Zheng, Shiqi Tian, Ailong Ma, Liangpei Zhang, and Yanfei Zhong. Scalable multi-temporal remote sensing change data generation via simulating stochastic change process. In *Proceedings of the IEEE/CVF International Conference on Computer Vision*, pages 21818–21827, 2023. 3
- [75] Zhuo Zheng, Stefano Ermon, Dongjun Kim, Liangpei Zhang, and Yanfei Zhong. Changen2: Multi-temporal remote sensing generative change foundation model. *IEEE Transactions on Pattern Analysis and Machine Intelligence*, 2024. 3
- [76] Zhuo Zheng, Yanfei Zhong, Ailong Ma, and Liangpei Zhang. Single-temporal supervised learning for universal remote sensing change detection. *International Journal of Computer Vision*, 132(12):5582–5602, 2024. 8

Remote Sensing Change Detection via Weak Temporal Supervision

Supplementary Material

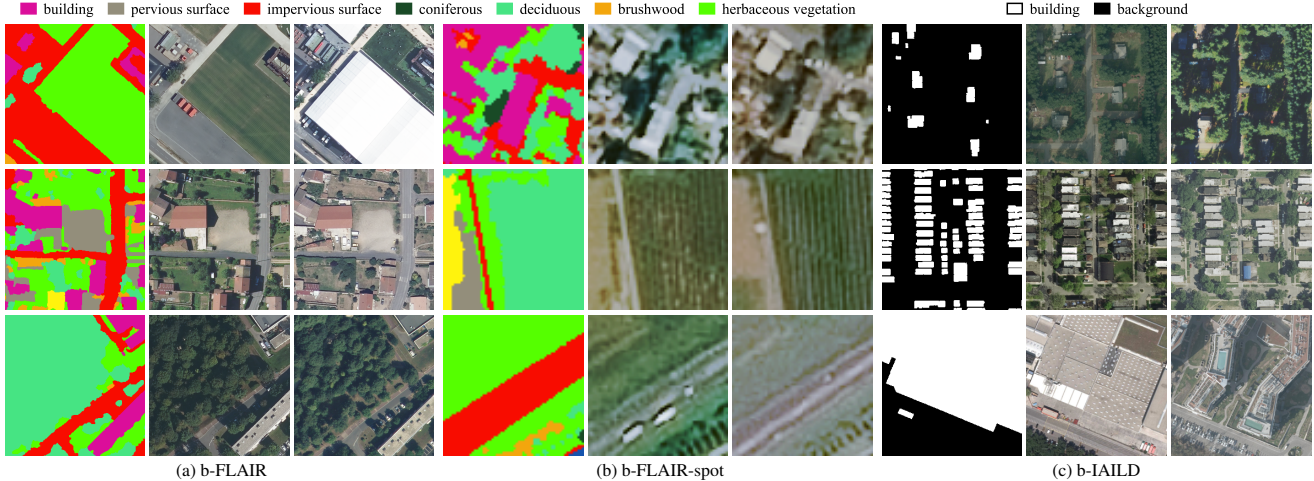


Figure A1. **Additional example triplets from our extended datasets**, b-FLAIR, b-FLAIR-spot, and b-IAILD, to complement the visual examples already displayed in Fig. 2 of the main paper. For each dataset, we show triplets $(S_t, I_t, I_{t'})$ in this order from left to right.

We first provide additional details on the datasets used in this work (Sec. A). Then we detail our implementation (Sec. B). Finally, we report supplementary quantitative and qualitative results (Sec. C). Our code and datasets will be released publicly for anyone to use.

A. Data

Fig. A1 shows further examples of triplets of bi-temporal images and their corresponding single-temporal semantic masks, for our three extended datasets, b-FLAIR, b-FLAIR-spot and b-IAILD. We describe them below, and also give a brief description of the benchmark datasets we used (LEViR-CD, WHU-CD and S2Looking).

A.1. b-FLAIR

The original FLAIR dataset is based on the French IGN’s BD ORTHO product [29] and its associated elevation data. For details on these data products, their pre-processing and their formatting into the FLAIR dataset, please refer to the FLAIR datapaper [25]. The BD ORTHO product is updated every three years on average at each location with new aerial acquisitions. This allowed us to extend FLAIR dataset with a new temporal acquisition for each of its 77,762 patches. For each patch, we extracted a 5-band (RGB, infrared, elevation) patch from the closest temporal acquisition of the BD ORTHO product and its associated elevation data, following the same process as described in [25]. We use the same training splits as in the original paper [26] (see Fig. A2),

except for the hyperparameter studies for which a subset of the data is used (departments 13, 21, 44, 63, 80 for training, and 77 for validation). The average number of days between two acquisitions is 1097 days (~ 3 years). 82.9% of our added images correspond to images acquired after the corresponding original FLAIR patches, while the remaining were acquired before. The average number of days between two acquisitions within the same calendar year is 44 (~ 1.5 months), with 18% of the pairs having more than a 3-month difference within the same calendar year, indicating possible significant seasonal variations for a given image pair. In addition, the differences in the time of the acquisitions within the day—which is 153 min on average—and in the angle of acquisition, introduce significant radiometric, geometric, and shadow-related variations.

A.2. b-FLAIR-spot

For all patch location and acquisition date of b-FLAIR, we download a corresponding SPOT-6/7 patch from the ORTHO-SAT database [31]. These are RGB images in 8 bits, at a spatial resolution of 1.5 m/px. We resized the patches at the shape 64×64 , resulting in an effective spatial resolution of 1.6 m/px. The ORTHO-SAT is an annual product, and we align the acquisition year of the images of b-FLAIR-spot on the corresponding images in b-FLAIR. This allows us to reuse FLAIR annotations for b-FLAIR-spot, provided a nearest-neighbor resampling from 512×512 to 64×64 .

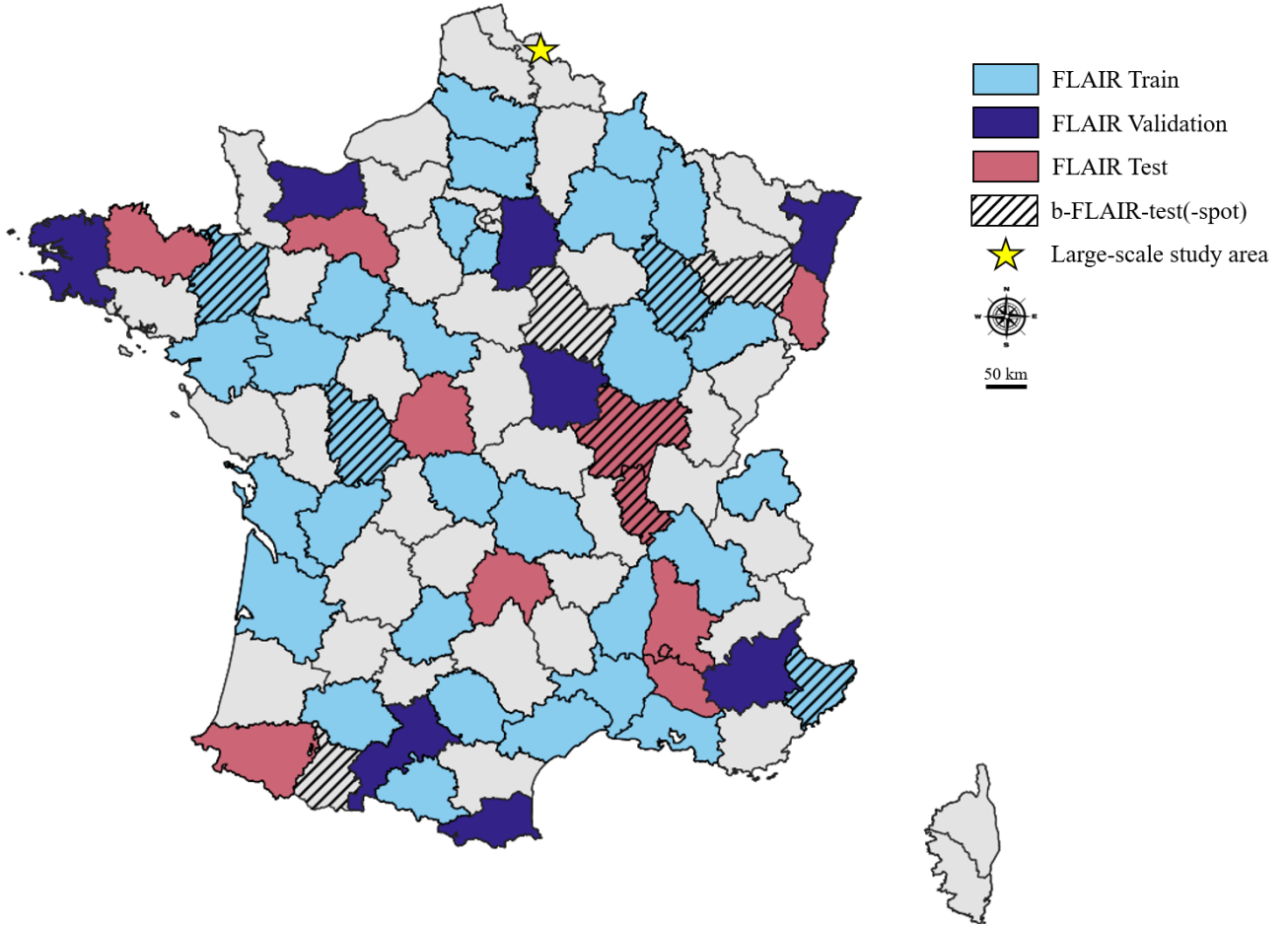


Figure A2. **Spatial repartition of b-FLAIR-test(-spot) data w.r.t. FLAIR**, within Metropolitan France. Note that even if pairs from b-FLAIR-test(-spot) are from departments already covered by FLAIR, we made sure that there is no intersection between the two datasets. We also indicate with a \star the location of the large-scale zone used for Fig. 1 of the main paper.

A.3. b-IAILD

The original IAILD [45] public training set is composed of images from 5 cities from the USA (Austin, Chicago, Kitsap) and Austria (Tyrol, Vienna). For each city, the dataset contains 36 tiles of size 5000×5000 px at the spatial resolution of 30 cm/px. We downloaded new acquisitions over the same locations from the USGS website¹ and the respective website of the Austrian provinces of Tyrol² and Vienna³. Years of acquisition of the new added orthophotographies are the following : 2024 for Vienna, 2023 for Chicago, Kitsap and Tyrol, and 2022 for Austin. Because the spatial resolution varies across the areas of interest (15 cm/px for Vienna, 20 cm/px for Tyrol, and 60 cm/px for Austin, Chicago and Kitsap), we resample all the downloaded tiles—as well as

the original IAILD tiles—at the common resolution of 60 cm/px. As in [45], we keep the first 5 tiles of each zone for validation, and use the other 31 for training. The resulting 2500×2500 images are split in 100 patches of size 256×256 , over a grid with an overlap of 6 pixels between adjacent cells. This results in a dataset containing 15500 training pairs (3100 per area) and 2500 validation pairs (500 per area).

A.4. b-FLAIR-test & b-FLAIR-test-spot

b-FLAIR-test is composed of 1730 image pairs annotated with a binary building change mask. The images are in the same 5-band 512×512 format as FLAIR images and were acquired, processed, and formatted following the procedure described in [25]. The images were extracted from 9 different French administrative departments and do not intersect the FLAIR dataset, which allows for a sound evaluation of methods trained on FLAIR or on our bi-temporal extension of FLAIR (see Fig. A2). The pairs were annotated by photo-

¹<https://earthexplorer.usgs.gov/>

²<https://data-tiris.opendata.arcgis.com/>

³<https://www.wien.gv.at/ma41datenviewer/public/start.aspx>

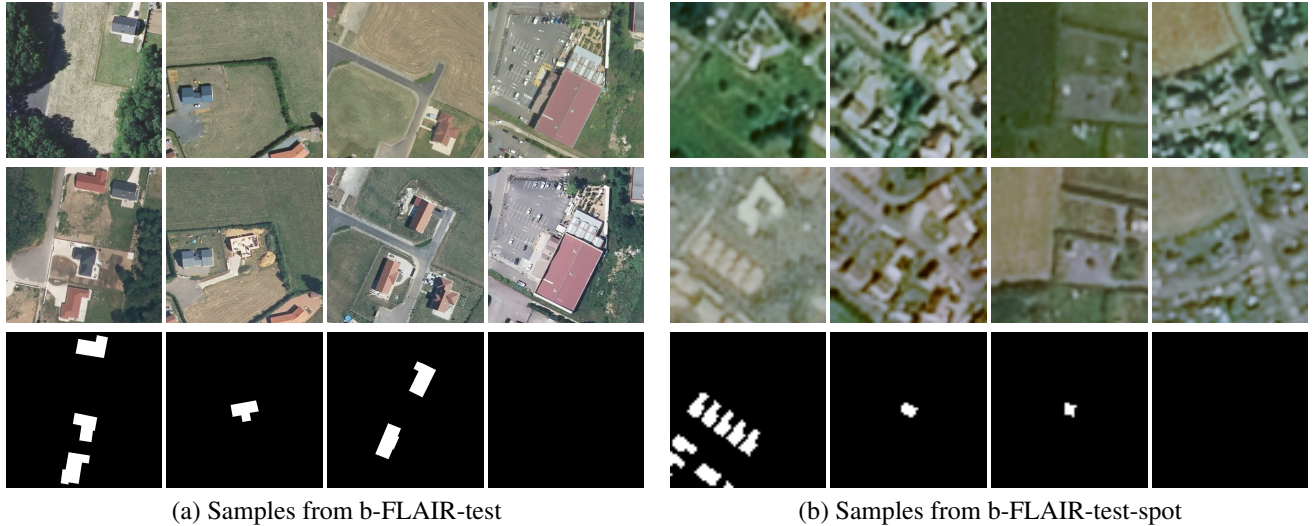


Figure A3. **Examples triplets of our test sets for building change detection.** We show additional example triplets (I_t , $I_{t'}$, M) in this order from top to bottom, for b-FLAIR-test (a) and b-FLAIR-test-spot (b).

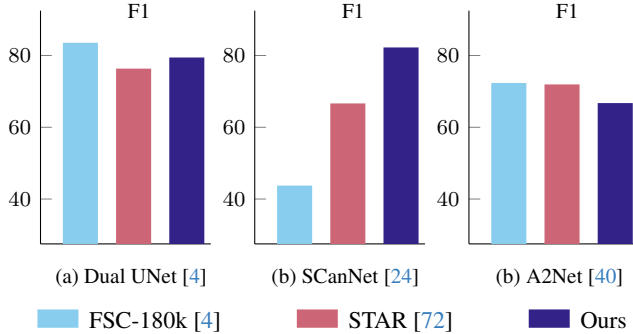


Figure C1. **Comparison with different architectures on b-FLAIR-test.** Like competing approaches, our methodology can be applied to any 3-branch change detection architecture.

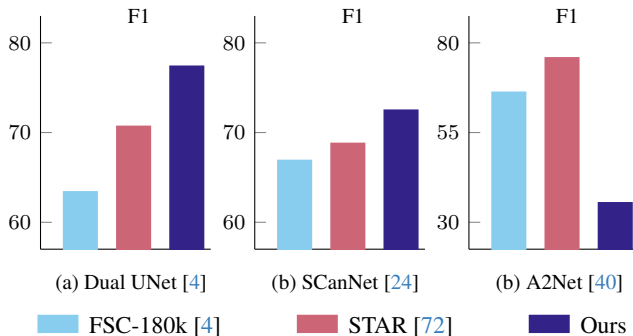


Figure C2. **Comparison with different architectures on WHU-CD.** Like competing approaches, our methodology can be applied to any 3-branch change detection architecture.

to interpretation experts and verified by a non-expert assessor. The pairs either show new building constructions, or no building change at all ($\sim 30\%$ of the pairs), but no pair exhibits building destruction. b-FLAIR-test-spot is built from b-FLAIR-test similarly as how we obtained b-FLAIR-spot based on b-FLAIR, *i.e.* by downloading acquisition at the same date and location for each patch, and downsampling the annotation masks. Example triplets for these two datasets can be visualized in Fig. A3.

A.5. LEVIR-CD, WHU-CD and S2Looking

LEVIR-CD [14] is composed of 637 pairs of aerial images of size 1024×1024 at the spatial resolution of 50 cm/px. We keep the original data splits (445 images for training, 64 for validation, and 128 for testing). LEVIR-CD’s images are from 20 different regions in the state of Texas, US, and were acquired between 2002 and 2018. The temporal gap for two acquisitions of the same location in the dataset range from less than a year to 15 years.

WHU-CD [33] is composed of 7620 pairs of aerial images of size 256×256 at the spatial resolution of 7.5 cm/px. We keep the original data splits (6096 images for training, 762 for validation, and 762 for testing). WHU-CD’s images are of the area of Christchurch, New Zealand, and were acquired in 2012 (pre-change) and 2016 (post-change).

S2Looking [54] is composed of 5000 pairs of satellite images of size 1024×1024 at a spatial resolution between 50 cm/px and 80 cm/px. We keep the original data splits (3500 images for training, 500 for validation, and 1000 for testing). S2Looking’s images are from 15 areas of interest spread across Europe, Asia, Africa, and North and South America.

Table A1. **Overview of benchmark datasets.** We report the main characteristics of the 5 evaluation datasets on which we compare our approach to the baselines.

Dataset	Modality	Resolution (cm/px)	Location	Image Size	Num. test pairs
LEVIR-CD [14]	Aerial	50	Texas, US	1024×1024	128
WHU-CD [33]	Aerial	7.5	Christchurch, New Zealand	256×256	762
S2Looking [54]	Satellite	50-80	Global	1024×1024	1000
b-FLAIR-test (ours)	Aerial	20	France	512×512	1730
b-FLAIR-test-spot (ours)	Satellite	160	France	64×64	1730

They were acquired between 2017 and 2020, with a temporal gap ranging from 1 to 3 years between bi-temporal acquisitions.

Tab. A1 summarizes the main characteristics of these three datasets, as well as those of our two datasets, b-FLAIR-test and b-FLAIR-test-spot.

B. Implementation details

A general diagram of the proposed weak temporal supervision approach is shown in Fig. B1. We trained the b-IAILD and b-FLAIR-spot models on a single NVIDIA RTX 6000 GPU with batch sizes of 64 and 256, respectively. Training the b-IAILD model required approximately 26 hours, while b-FLAIR-spot completed in about 5.5 hours. The b-FLAIR dataset contains a significantly larger number of pixels than the other datasets, resulting in substantially higher computational complexity. Consequently, we trained the b-FLAIR models on a multi-GPU setup with 32 NVIDIA V100 GPUs and a batch size of 32, where a complete training took roughly 4 hours. For all models, we use image crops of 256×256 pixels (except b-FLAIR-test, for which images are of size 64×64) and normalize input images using the per-channel mean and standard deviation computed over the entire training dataset, following Benidir *et al.* [4]. During inference and evaluation, target images are normalized using the same statistics as the training set.

In Fig. B2, we show example of change maps generated with our implemented sIoU-based methods. We visually compare them to change maps computed with logical operations (OR and XOR). While XOR-based masks leave residual change pixels around almost-overlapping buildings, our masks ignore such pixels, though they may correspond to an actual difference in land cover. We believe these “cleaner”, object-based change masks constitute a better supervision in order to train models that are less prone to false alarms.

C. Additional Results

This section provides additional quantitative and qualitative results that complement those of the main paper.

C.1. Different architectures

Figures C1 and C2 report the performance of our method using three different architectures: Dual UNet [4], SCanNet [24], and A2Net [40]. A2Net is a lightweight model with 3.52 M parameters, SCanNet contains 27.9 M parameters, while Dual UNet is the largest architecture with 65.05 M parameters. Figure C1 presents the F1 scores on the b-FLAIR-test split for the FSC-180k [4] approach, the STAR [72] baseline and our method. Figure C2 reports the same evaluation in a zero-shot setting on the WHU-CD dataset. Our method achieves competitive performance when using Dual UNet and SCanNet backbones across both datasets. In contrast, A2Net performs poorly on WHU-CD. We attribute this behavior to its limited model capacity, which induces a strong bias toward the *no-change* class. This observation is consistent with the large discrepancy in parameter counts between A2Net (3.5 M) and the larger Dual UNet (65.1 M) and SCanNet (27.9 M) architectures.

C.2. Large-scale results

In Fig. 1 of the main paper, we present large-scale results over the metropolitan area of Lille, France (approximately 55.3 km^2 , see Fig. A2 for location on France map). This section provides additional details on the inference setup and extends the analysis to SPOT-6/7 satellite imagery.

The large-scale inference on Lille uses BD ORTHO [29] bi-temporal aerial images from 2018 and 2021. We extract 512×512 crops with a 6-pixel overlap and feed them to our model pre-trained on b-FLAIR, as well as to the FSC-180K model of Benidir *et al.* [4]. A 5×5 spatial median filter is applied to the model outputs.

Motivated by the strong performance on very high-resolution aerial data, we also evaluate our method at scale on more widely accessible satellite imagery. We extract 64×64 SPOT-6/7 crops from IGN’s ORTHO-SAT database [31] at 1.5 m/pixel resolution with a 5% overlap. We process these crops with the same inference pipeline and report results for both our b-FLAIR-spot model and its STAR counterpart in Fig. C3. As shown, the STAR model produces many false positives, similar to FSC-180K on the BD ORTHO experiment. In contrast, our model is substantially more robust to false alarms and successfully highlights most

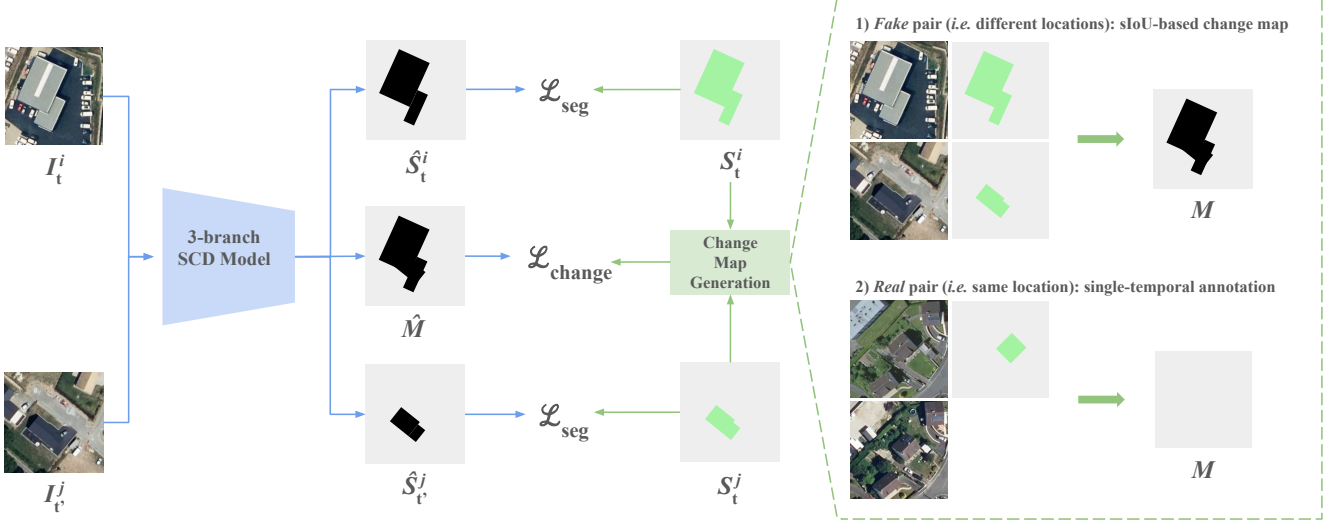


Figure B1. General diagram of the proposed methodology. Our methodology can be applied to any 3-branch SCD model, provided it can take two images at different dates as input and produce a semantic segmentation mask for each date, and a change mask. The semantic segmentation task is supervised through the single-temporal available ground truth, implying a temporal augmentation on the additional non-annotated image. The change detection task is supervised via weak temporal augmentation, creating *fake* change examples by pairing images of different locations, and no-change examples by assuming no changes occurred between *real* pairs.

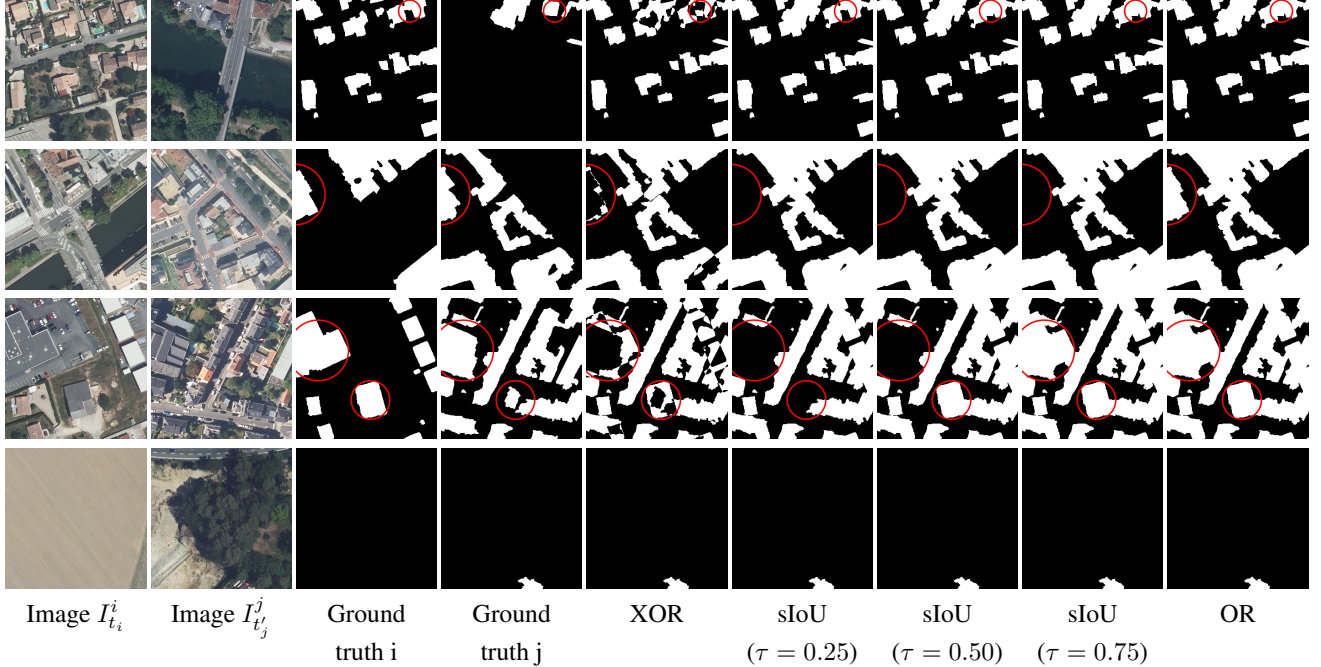


Figure B2. Example of generated change maps for pairs of images of b-FLAIR from different locations, with a focus on the “building class”. We show maps resulting from logical operations (XOR or OR) as well as sIoU-based maps computed for various values of the threshold τ . We highlight with red circles, areas for which differences in building footprints between the two images are variably considered as changed or not depending on the method.

large change regions, although it remains more susceptible to false negatives.

C.3. Additional qualitative results

Tab. C1 provides additional FPR results for all evaluated methods as an extension of the results presented in the main

Table C1. **Comparison with baselines.** Similar to the table from the main paper but with the false positive rate reported for all methods. Best score for each training data source is highlighted in bold, and the second best score is underlined.

Data source	Model	Dataset extension	In-domain						Out-of-Domain								
			b-FLAIR-test			b-FLAIR-spot-test			LEVIR-CD			WHU-CD					
			$F1 \uparrow$	$IoU \uparrow$	$FPR \downarrow$	$F1 \uparrow$	$IoU \uparrow$	$FPR \downarrow$	$F1 \uparrow$	$IoU \uparrow$	$FPR \downarrow$	$F1 \uparrow$	$IoU \uparrow$	$FPR \downarrow$			
FLAIR	UNet	—	62.6	45.5	3.09	—	—	—	31.9	19.0	2.11	62.0	44.9	5.00	12.1	6.5	2.21
	UNet	b-FLAIR	65.2	48.3	2.69	—	—	—	35.3	21.4	<u>2.10</u>	65.2	48.3	4.37	12.5	6.7	1.34
	Dual UNet	FSC-180k [4]	83.1	71.1	<u>0.73</u>	—	—	—	49[†]	33[†]	—	63.3	46.3	3.66	4 [†]	2 [†]	—
	Dual UNet	—	75.9	61.1	1.49	—	—	—	37.5	23.1	2.64	70.6	54.5	3.32	13.7	7.4	0.72
	Dual UNet	b-FLAIR	79.0	65.3	0.35	—	—	—	17.8	9.3	0.30	77.3	63.0	0.77	<u>13.6</u>	<u>7.3</u>	0.58
FLAIR-spot	UNet	—	—	—	—	24.1	13.7	6.78	3.0	1.5	<u>0.49</u>	15.2	8.2	6.14	0.4	0.2	<u>0.06</u>
	UNet	b-FLAIR-spot	—	—	—	<u>25.0</u>	<u>14.3</u>	6.02	<u>19.5</u>	<u>10.8</u>	13.3	<u>28.6</u>	<u>16.7</u>	10.1	<u>1.9</u>	<u>1.0</u>	0.32
	Dual UNet	—	—	—	—	29.2	17.1	<u>4.83</u>	0.7	0.4	0.12	5.2	2.7	1.12	0.1	0	0.02
	Dual UNet	b-FLAIR-spot	—	—	—	22.9	12.9	<u>0.31</u>	34.1	20.6	4.04	49.3	32.7	<u>3.42</u>	7.1	3.7	1.57
IAILD	UNet	—	—	—	—	—	—	—	53.1	36.2	3.0	42.6	27.1	10.1	4.6	2.4	19.7
	UNet	b-IAILD	—	—	—	—	—	—	44.9	28.9	<u>1.8</u>	44.5	28.6	8.1	<u>7.9</u>	<u>4.1</u>	<u>9.7</u>
	Dual UNet	—	—	—	—	—	—	—	54.7	37.6	3.3	<u>53.7</u>	<u>36.7</u>	<u>7.1</u>	6.1	3.1	12.7
	Dual UNet	b-IAILD	—	—	—	—	—	—	35.9	21.9	<u>0.3</u>	63.3	46.3	1.9	17.6	9.6	2.4
Dual UNet	SyntheWorld [56]	—	—	—	—	—	—	—	25 [†]	13 [†]	—	25.1	14.3	11.2	0 [†]	0 [†]	—

Table C2. **Performance across training iterations.** F1 Score (%) and IoU (%) of our method over three training iterations using the *b-FLAIR-spot* dataset. Best results per dataset are shown in bold. The numbered of filtered pairs with respect to the training dataset is indicated for each iteration.

Iteration	Filtered Samples	In-domain						Out-of-Domain					
		b-FLAIR		b-FLAIR-spot		b-IAILD		LEVIR-CD		WHU-CD		S2Looking	
		F1	IoU	F1	IoU	F1	IoU	F1	IoU	F1	IoU	F1	IoU
Iteration 1	0	67.3	50.7	—	—	—	—	5.2	2.7	51.8	34.9	10.5	5.6
Iteration 2	484	78.1	64.1	—	—	20.3	11.3	76.1	61.4	15.4	8.3	—	—
Iteration 3	842	79.0	65.2	—	—	17.8	9.3	77.3	63.0	13.6	7.3	—	—
b-FLAIR-spot													
Iteration 1	0	—	—	22.6	12.7	—	—	34.3	20.7	48.6	32.1	6.9	3.2
Iteration 2	148	—	—	21.7	12.2	35.4	21.5	47.2	30.9	5.5	2.8	—	—
Iteration 3	287	—	—	22.9	12.9	34.11	20.6	49.3	32.7	7.1	3.7	—	—
b-IAILD													
Iteration 1	0	—	—	—	—	57.2	40.1	66.9	50.2	14.5	7.8	—	—
Iteration 2	49	—	—	—	—	34.4	20.8	67.9	51.4	14.7	8.0	—	—
Iteration 3	41	—	—	—	—	35.9	21.9	63.3	46.3	17.6	9.6	—	—

paper. Our method consistently leads to less false positive than baselines, though performing on par with them w.r.t other metrics on most datasets. This is especially the case on in-domain datasets and on WHU-CD. In Fig. C4, we can clearly see that, on b-FLAIR-test-spot, our method mostly predict no change, whereas its change predictions are accurate (see first row). On the contrary, the other methods show a significant number of false alarms, making them unusable in practical applications. This behavior can also be observed with the zero-shot qualitative results on LEVIR-CD (Fig. C5) and WHU-CD (Fig. C6). On S2Looking (Fig. C7), all methods globally perform poorly due to the important domain gap with the training data.

C.4. Detailed impact of the iterative refinement

Tab. C2 reports the results for each iteration of our models trained on b-FLAIR, b-FLAIR-spot, and b-IAILD, respectively. Although we set the hyperparameter $N_{\text{iter}} = 3$ based solely on in-domain dataset results, we also report the impact of iterative refinement on out-of-domain zero-shot performance. With the exception of the b-IAILD model on LEVIR-CD, where the first iteration significantly outperforms subsequent ones, removing detected change pairs from the dataset generally benefits out-of-domain performance. The number of filtered pairs at each iteration suggests that additional iterations could further improve model performance. However, given the marginal improvement between the second and third iterations on in-domain evaluation and considering computational cost constraints, we did not explore values of

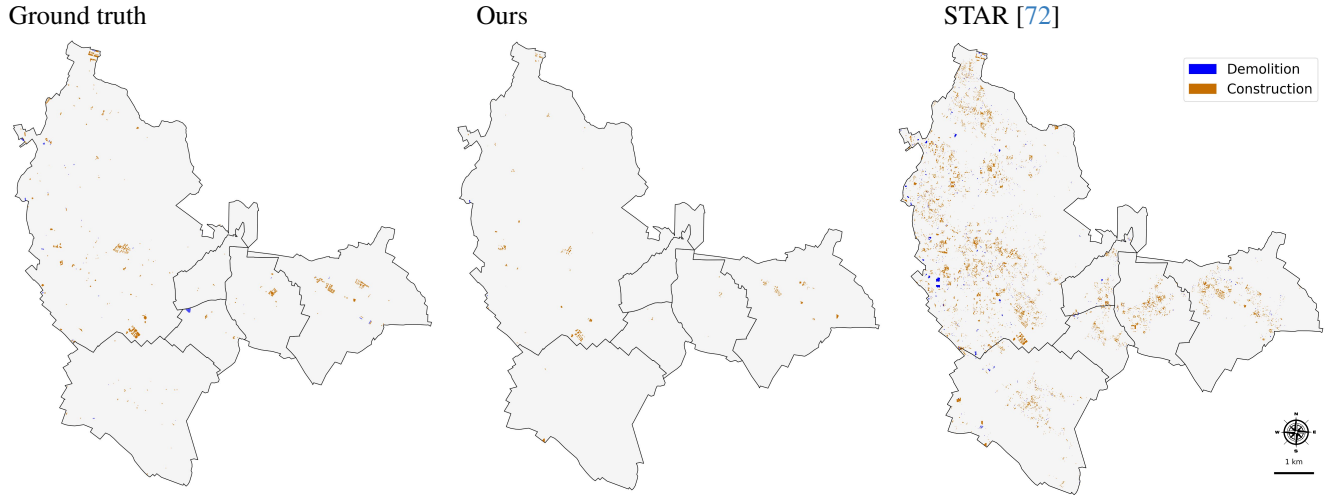


Figure C3. Large-scale SPOT-6/7 change detection results. Comparison between ground truth, our b-FLAIR-SPOT model, and the STAR approach over the metropolitan region of Lille, France. While our model predicts a considerable number of false negatives, it detects most areas where larger changes were produced, while the STAR version detects an overwhelming amount of false positives.

N_{iter} greater than 3.

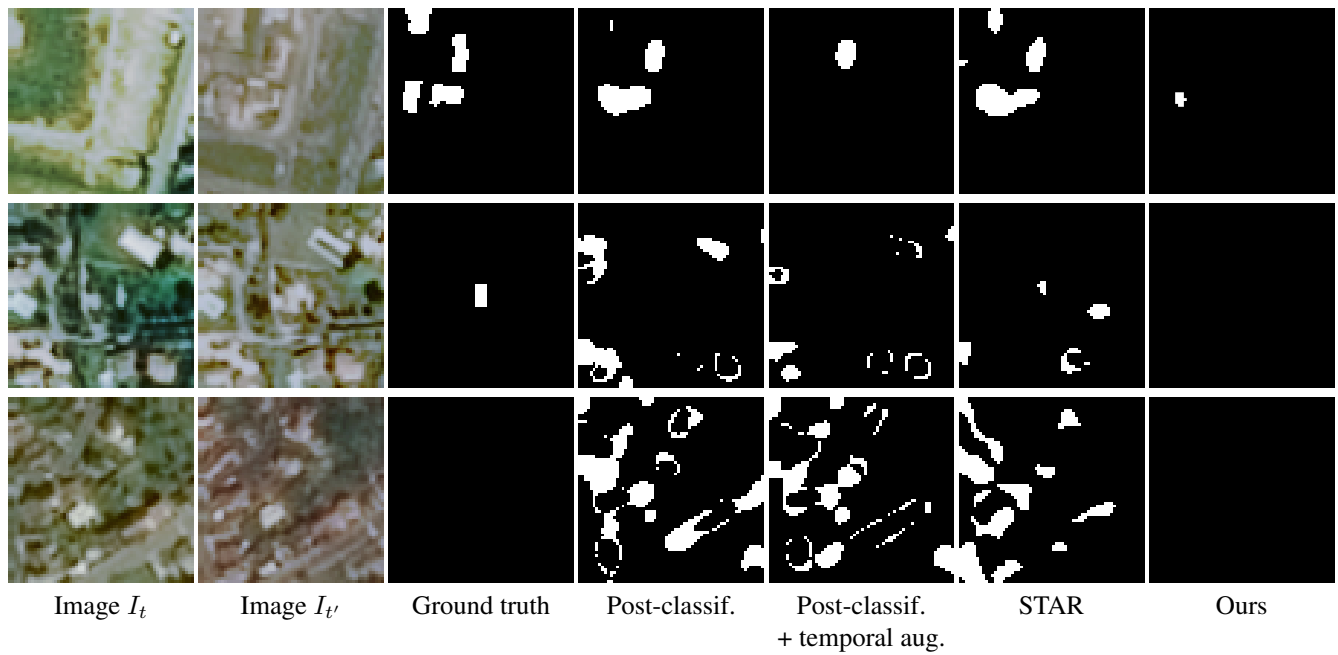


Figure C4. **Qualitative results on b-FLAIR-spot-test.** We compare the building change maps predicted by baseline methods and ours.

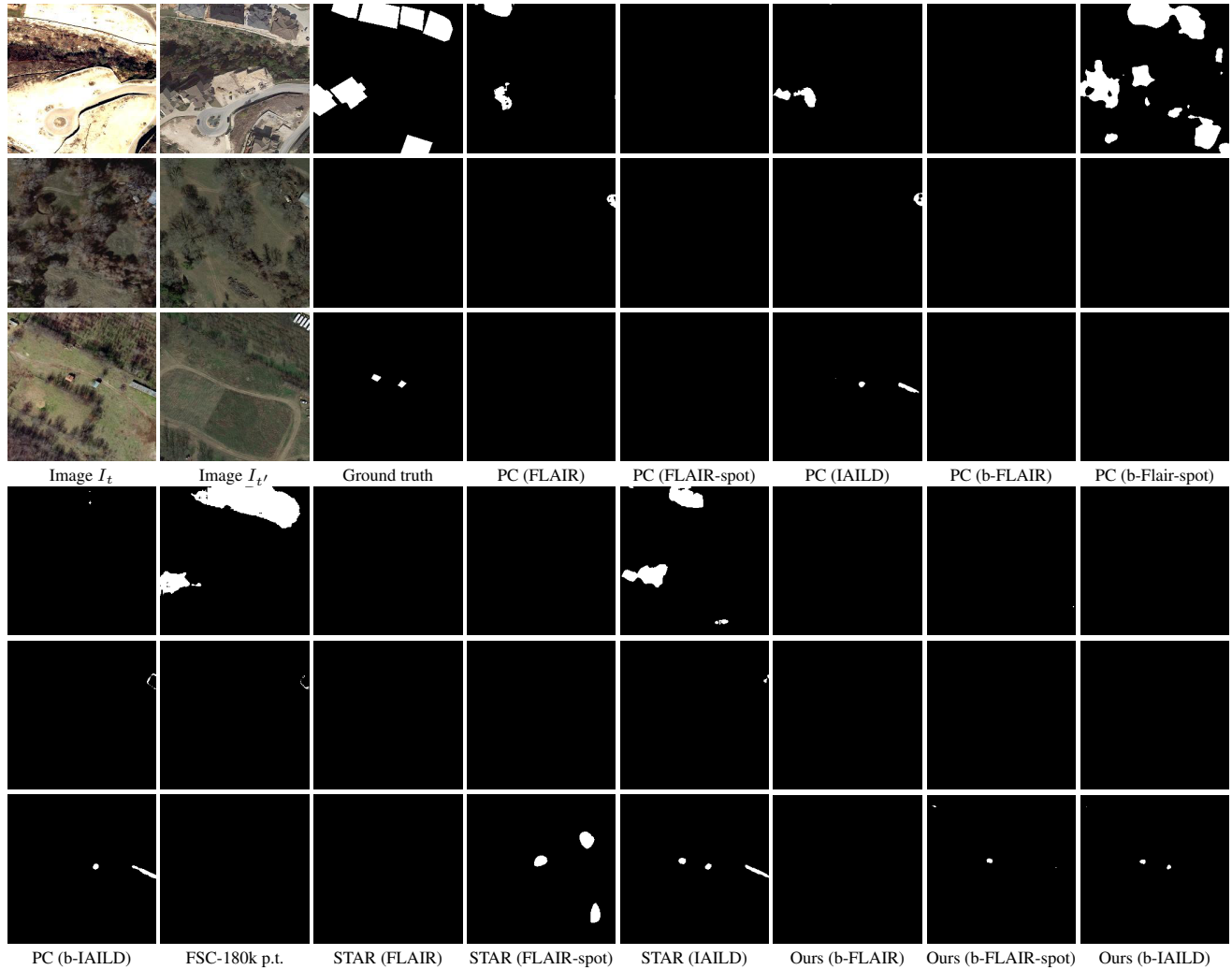


Figure C5. **Qualitative zero-shot results on LEVIR-CD** for 3 randomly selected input pairs. “PC” stands for “post-classification” and “p.t.” for “pre-training”.

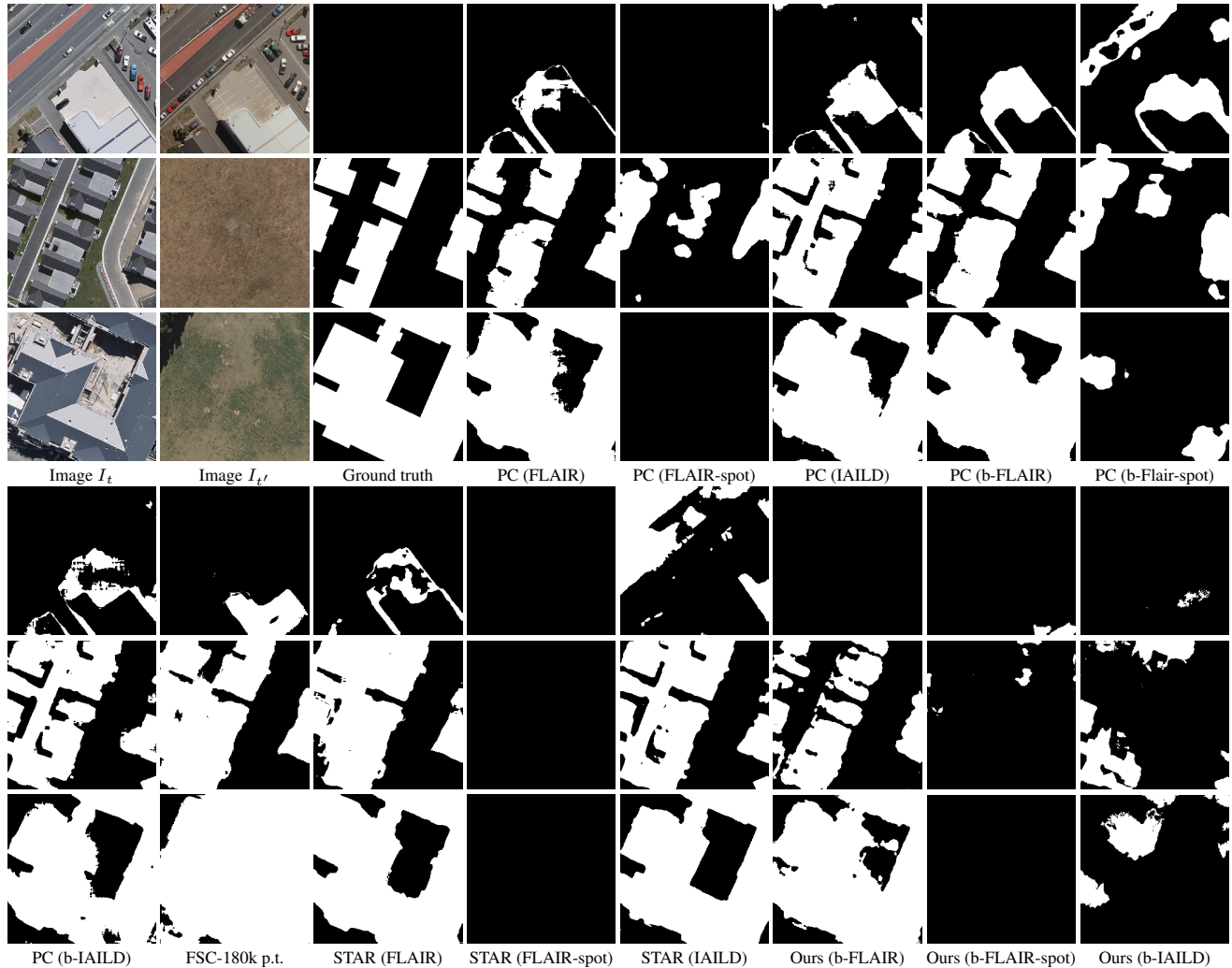


Figure C6. **Qualitative zero-shot results on WHU-CD** for 3 randomly selected input pairs. “PC” stands for “post-classification” and “p.t.” for “pre-training”.

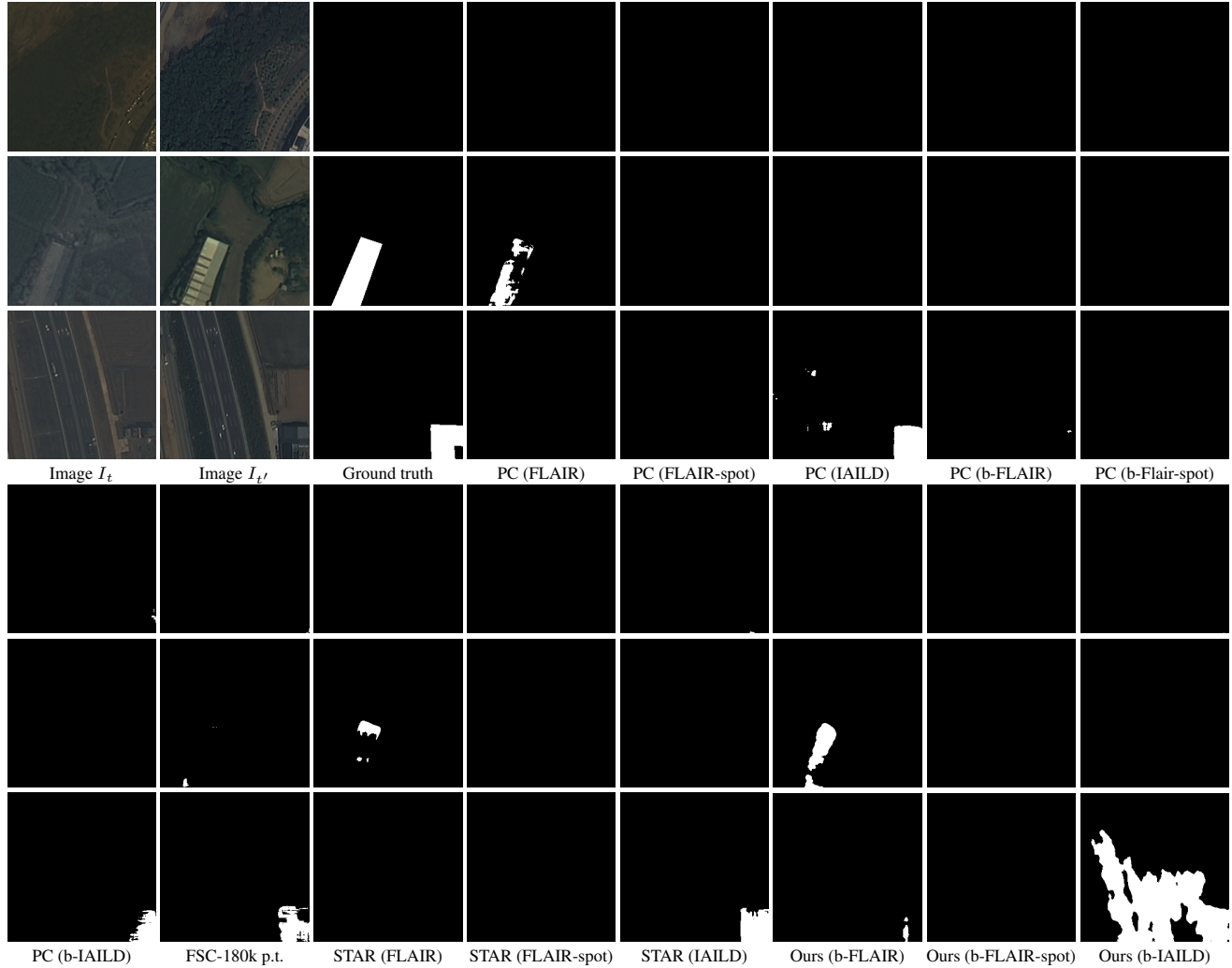


Figure C7. **Qualitative zero-shot results on S2Looking** for 3 randomly selected input pairs. “PC” stands for “post-classification” and “p.t.” for “pre-training”.